Statistical Kinetics of Actin Filament Nucleation studied with Zero-Mode Waveguides

Masterarbeit aus dem Fachgebiet

Physikalische Chemie

von

cand. chem. Maria Hoyer

geboren am 17.09.1989 in Berlin

für die Masterprüfung in Biochemie an der

Ludwigs-Maximilians-Universität München

Datum der mündlichen Prüfung: 09.05.2014

Beginn derMasterarbeit: 02.06.2014

Masterarbeit beim Prüfungsausschuss eingereicht am 02.12.2014

Erklärung

Ich versichere, dass ich die vorgelegte Masterarbeit am Institut für physikalische Chemie im Arbeitskreis Prof. Don C. Lamb unter der Anregung und Anleitung von Dr. Alvaro H. Crevenna selbstständig durchgeführt und keine anderen als die angegebenen Hilfsmittel und Quellen benützt habe.

München, 02.12.2014, ...

Erstgutachter: Prof. Don C. Lamb

Zweitgutachter: Prof. C. Bräuchle

Thank you

Ruth Hoyer

Monika Manghabati

Alvaro Crevenna

O'car Campos

Kyra Hoyer

Jakob Gaar

Sushi Madhira

Hannes Hoyer

Waldemar Schrimpf

Patrick Hoyer

Don Lamb

David Manghabati

Fabian Wehnekamp

Ioanna Savcheva

Philipp Messer

Pia Hoyer

Anna-Lena Cost

Lena Voithenberg

Contents

1 Introduction **6**

1.1 Biochemical Background 7

1.1.1 From monomeric to filamentous Actin 7

1.1.2 Gelsolin 8

1.1.3 DNase I Binding to Actin 12

1.1.4 Inhibition of Filament Formation by Latrunculin A 12

1.2 Fluorescence Spectroscopy 13

1.3 Zero-mode waveguides 14

1.4 Step-finding Algorithms 16

1.4.1 Kalafut-Visscher Algorithm 17

1.4.2 L1-regularized Global Step-smoothing 18

1.4.3 Step-finding according to Salapaka 18

1.5 Single-molecule Kinetics and Mechanisms 19

1.6 Objectives 20

2 Materials and Methods **22**

2.1 Wide-Field Microscopy Set-up 22

2.2 Sample Preparation 22

2.2.1 Actin Nucleation Assays 22

2.2.2 DNA Measurements 23

2.3 Analysis 23

3 Results **25**

3.1 Comparison of Step-finding-algorithms 25

3.1.1 Kalafut-Visscher 26

3.1.2 L1KV 27

3.1.3 Salapaka 29

3.1.4 L1KV and Salapaka applied to Actin Polymerization 31
3.1.5 Discussion 34
3.2 Gelsolin-mediated Pointed-end Filament Nucleation 38
3.3 Barbed End Nucleation 46
3.3.1 Nucleation on biotinylated Actin 46
3.3.2 DNase I mediated Nucleation 47

4 Discussion **51**

5 Summary **56**

Bibliography **57**

Appendix **66**

1 Introduction

The organization of the cytoskeleton is essential for many cellular processes, such as motility, trafficking, endocytosis, cell shape and polarity of the cell [1]. In response to growth factors or chemoattractants in the environment, the actin cytoskeleton undergoes dramatic changes. This involves disassembly of the existing meshwork as well as nucleation of new filaments, i. e. the transition of globular (G) to filamentous (F) actin. Despite its important role, the mechanisms of actin nucleation are poorly understood. In 2009, a new model of the actin filament has been proposed which involves flattening of the actin monomer during the monomeric to filamentous state transition [2]. Thus, the beginning and the end points of the structural transition are known, however, the mechanisms and kinetics of the transition remain elusive. The direct measurement of the incoming single actin monomers to a nucleating filament would provide insight into these questions. For this purpose, single-molecule sensitivity is necessary. Confocal fluorescence microscopy or total internal reflection microscopy in principle provide the possibility to measure single molecules. However, for these techniques very low concentrations are needed. The critical concentration for actin filament growth at the pointed end is at 0.6 μM [3]. Single-molecule measurements in the micromolar range need smaller observation volumes than confocal microscopy can provide.

There are several strategies to overcome the diffraction limit. This year's Nobel prize in chemistry was given to Eric Betzig, William Moerner and Stefan Hell for their contributions to fluorescence microscopy at resolutions beyond the diffraction-limit [4–7]. They developed techniques based on the timewise or spectral separation of the signal of single fluorescent dyes to obtain nanometer resolution. These methods are helpful for the visualization of cellular structures and mechanisms, however, for photo-activated localization microscopy (PALM) and stochastic optical reconstruction microscopy (STORM), the studied structures need to be fixed. For molecules in solution, near-field scanning optical microscopy would be a way

to reach a sufficiently small observation volume. Here, the light-source itself is in the nanometer scale. Zero-mode waveguides are theoretically the inversion of this principle. Instead of minimizing the light source, the observation volume is confined by the architecture of the waveguides [8]. By using an array of zero-mode waveguides, several hundred individual molecules can be measured at once, which results in significant statistics.

In this thesis, actin filament nucleation and elongation in the barbed and pointed end direction was directly visualized using zero-mode waveguides. For this purpose, an actin-binding tethering protein has been fixed at the bottom of the waveguides. Using nearly 100% labeled actin monomers, the binding of those to the tethering protein could visualized directly in the intensity trace. Using step-finding algorithms, the arrival times of the individual actin monomers could be extracted from the measured traces. The high statistics of the data allows the further interpretation of the arrival time histograms along the lines of statistical kinetics.

Statistical kinetics can reveal the underlying enzymatic mechanisms of a biological system [9]. The shape of the arrival time distribution of a biochemical binding reaction provides information on the number of kinetically relevant states the system has to pass to successfully complete the reaction. Applied to actin nucleation, this would give insight into the structural rearrangements of the monomers and the respective binding protein.

1.1 Biochemical Background

1.1.1 From monomeric to filamentous Actin

Monomeric actin is composed of two major subunits, which can be further divided into two subunits each (Fig. 1.1 A) [10]. The interface between the major subunits form the nucleotide binding pocket. The equilibrium between the globular and filamentous form of actin depends on the state of the bound adenosine nucleotide [11–13]. ATP- and ADP-P_i-bound actin is more stable in filamentous form than the ADP-bound state [14].

Binding of ATP induces several conformational changes in subdomain 2 of actin compared to the ADP-bound state. These changes may result in a transition of the DNase binding loop from an α-helix to a disordered loop structure when ATP or ADP-P_i is bound [11, 15, 16]. Molecular dynamics simulations implied that the nucleotide binding cleft remains closed in the ATP- and ADP-P_i-bound states, but prefers an open conformation after P_i is released [16].

Whereas monomeric actin hydrolyses the bound ATP at a very slow rate, the filamentous form does so several orders of magnitude faster [15,17].Oda et al. proposed a model of filamentous actin where flattening of the actin monomers is assumed upon polymerization [2]. This would bring the potentially attacking water-coordinating residue Gln137 into closer proximity to the ATP [11, 12, 18]. The Oda model proposes a relative twist of the two major actin subunits of about 20°, which results in a flat conformation (Fig. 1.1). Additionally, a rearrangement of the DNase binding loop towards an open loop conformation is proposed. Alternatively, the loop in the helical conformation could extend into the upper actin monomer in the filament. Both the Oda and the earlier Holmes models show a helical arrangement of the actin monomers in the filament [2, 19, 20]. The major difference between the Oda and the Holmes model of 1990 are the distances between the two strands, which are closer together in the Oda model. This results in a more stable filament structure with more contacts between the actin subunits.

The two ends of the actin filament have different properties and are called the pointed and the barbed end. The faster elongation rate at the barbed end leads to the "treadmilling" effect *in vitro*, where monomers dissociated from the pointed end get incorporated again at the barbed end [21]. Polymerization rates for barbed end and pointed end elongation are 11.6 $\mu M^{-1}s^{-1}$ and 1.3 $\mu M^{-1}s^{-1}$, respectively, with bound ATP [3].

1.1.2 Gelsolin

Gelsolin is part of a superfamiliy of multidomain proteins that bind to and regulate actin in a Ca^{2+}-dependent manner [23]. It was first discovered to play a role in the

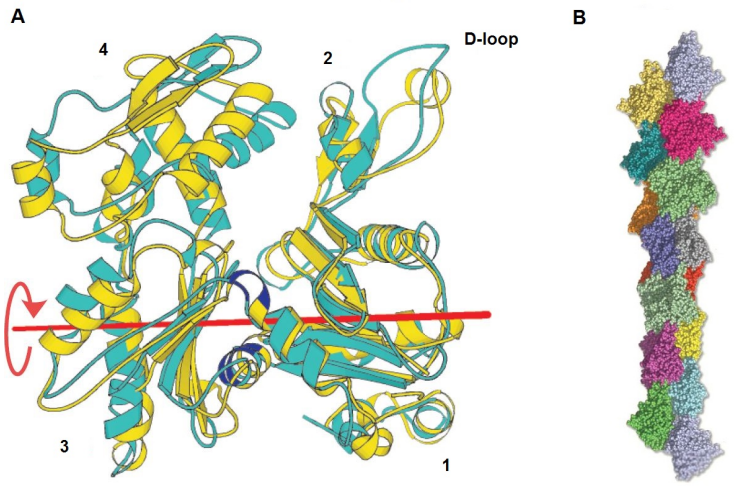

Figure 1.1: **Monomeric and filamentous actin. A:** Superposition of the filamentous actin structure according to Oda et al. (cyan) and tetramethylrhodamine-conjugated monomeric actin structure (yellow). Subdomains 3 and 4 are rotated with respect to subdomains 3 and 4 along the indicated red axis. **B:** Actin filament structure according to the Oda model. Each subunit is marked in a different colour. In the middle of the filament, one subunit is marked grey/blue according to the subunits facing the inner or the outer part of the filament, respectively. Adapted from [2, 22], (PDB: 2ZWH).

gel-sol transition of macrophage extracts [24, 25]. Besides its severing function of F-actin, it can cap filaments, sequester G-actin and nucleate filaments in *vitro*.

Gelsolin is composed of six structurally similar domains, G1 to G6, named according to their position on the peptide from the N- to the C-terminus. These gelsolin domains form a 5- to 6-stranded β-sheet between two α-helices, a long one approximately parallel to the β-strands and a short one perpendicular to them (Fig. 1.2) [26]. There are two different types of Ca^{2+} binding sites. Type-1 binding sites are located at the actin-binding interfaces in G1 and G4. The type-2 site is formed by the beginning of the long α-helix and the C-strand of the β-sheets (Fig. 1.2 B) and is conserved in the six gelsolin domains [27].

Inactive Gelsolin Conformation Gelsolin in the cytoplasma adopts an inactive state until needed. The inactive structure is formed by the compact assembly of G1 to G5 around G6, such that the three actin-binding sites are occluded (Fig. 1.3) [26]. Thereby, the protein divides itself into two pseudosymmetric halves, the domains G1, G2 and G3 being sequentially and structurally most similar to the domains G4,

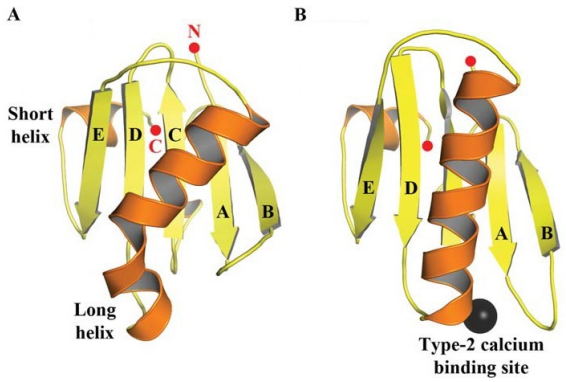

Figure 1.2: **The Gelsolin domain. A:** G3 as an example for a gelsolin domain in its inactive form. The long helix of G3 and G6 is kinked in the inactive conformation. β-sheets are labeled A through E, red dots mark the N- and C-termini. **B:** G3 in its active conformation with a straight helix with bound Ca^{2+} indicated in black. Adapted from [23] (PDB 1D0N).

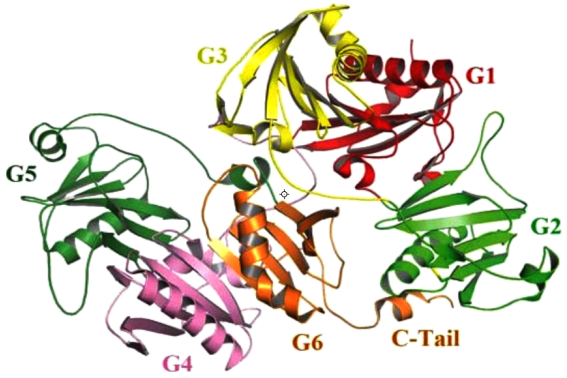

Figure 1.3: **The inactive conformation of Gelsolin.** From [23].

G5 and G6, respectively. The inactive structure is steadied by three latches [26–30]. The interaction of the long G2-α-helix with the C-terminal tail attached to G6 forms the C-terminal tail latch (Fig. 1.4 A), the G1-G3 latch is formed by their adjacent β-sheets and interactions between their E-strands (Fig. 1.4 B), similar to the G4-G6 latch (Fig. 1.4 C).

Gelsolin Activation Upon Ca^{2+} binding, the latches open, giving way to large conformational changes that result in symmetry-loss and the solvent accessibility of all actin-binding sites (Fig. 1.4). The release of the C-terminal tail from G2 exposes its F-actin binding site. The G3-G4 linker adopts an extended conformation, allowing the G1 to G3 domains to separate from G4 to G6 (Fig. 1.4 A). Subsequently, the

G1-G3 and G4-G6 latches open, followed by a complete repositioning of the domains (Fig. 1.4 B, C) [27,29,31]. As a result, G2 and G3 come closely together with G1 remotely attached via a linker region, its actin binding site exposed. In the C-terminal half, G6 gets displaced by 40 Å and 90°C to the opposite site of G5, thus releasing the actin-binding site of G4. Ca^{2+} activation is needed for this rearrangement, but not necessarily actin [31–33].

Ca^{2+} binding is thought to have the following effects: type-2 Ca^{2+} binding to G6 straightens the long α-helix (Fig 1.2) [34]. The resulting steric clashes help to release the G4-G6 latch and the N- and the C-terminal halves move apart. The new distance can allow for the straightening of the G3 long helix and subsequent opening of the G1-G3 latch (Figs. 1.2, 1.4 B). While the C-terminal half requires the occupation of additional Ca^{2+} binding sites to reach the active conformation, the N-terminal half can do so without additional Ca^{2+} [35–38]. For maximum severing efficiency of the N-terminal half, however, additional calcium is needed, indicating an activational role of actin itself [39–41]. Stabilization of the active conformation by actin also explains the high concentrations of calcium needed to achieve the fully active conformation in absence of actin, 0.2 to 1 mM in bulk assays, which does not occur inside cells [30,42,43]. Actin can change the Ca^{2+}-binding affinity of Gelsolin and trigger activating conformational rearrangements [29,35,39,43,44].

Binding to monomeric Actin Gelsolin binds two actin monomers in a ternary complex [45]. The actin monomer bound to the C-terminal half of gelsolin is easily exchangeable and binds with a slow rate constant of 0.015 to 0.07 $\mu M^{-1}s^{-1}$, dependent on pH [45–48]. It can bind after the initial activation of gelsolin at 0.1. - 1 μM Ca^{2+} [43,49–51]. The binding of the second actin monomer to the isolated N-terminal half is independent of Ca^{2+}, however, a stable complex with two actin monomers needs Ca^{2+} concentrations above 10 μM [51]. The second monomer binds with a rate constant of 2 $\mu M^{-1}s^{-1}$ and has a dissociation rate of 0.02 s^{-1} [52]. It is believed that the binding of the second actin needs further structural rearrangements of the C-terminal half of gelsolin that occur at high Ca^{2+} concentrations, possibly promoted by binding of the first monomer [36,51].

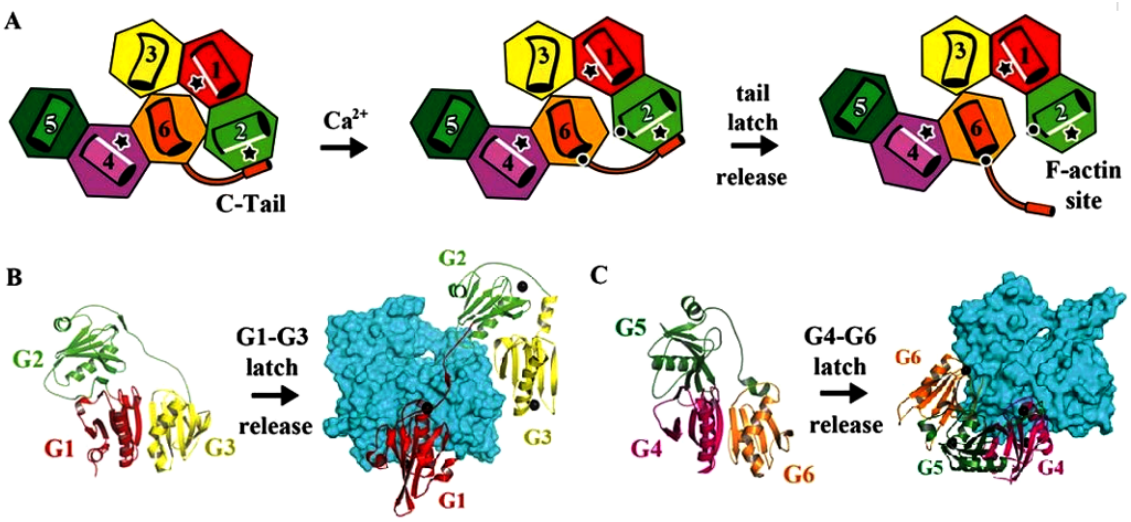

Figure 1.4: **The opening of the three latches. A:** C-terminal latch, **B:** G1-G3 latch, **C:** G4-G6 latch. Cartoon representation: Subunits are color-coded according to the crystal structures. Cylinders represent the long α-helices (white sites: actin-binding regions, with stars: major binding regions). Adapted from [23].

The monomer bound to the N-terminal half undergoes conformational changes in the complex, involving the DNase I binding loop and the C-terminus [47].

1.1.3 DNase I Binding to Actin

DNase I forms a stable stoichiometric complex with monomeric actin, which inhibits the nuclease activity of the DNase and leads to actin filament depolymerization by shifting the G-F equilibrium [53]. It binds to the pointed end of actin (Fig. 1.5 A), prohibiting filament formation in that direction [10]. Studies using digestion assays or Förster resonance energy transfer showed that alterations of the DNAse binding loop in subdomain 2 of actin induces allosteric conformational changes in subdomain 1 [54, 55].

1.1.4 Inhibition of Filament Formation by Latrunculin A

Latrunculin A and B are toxins purified from the Red Sea sponge *Latrunculia magnifica*. They have a macrolide-based structure (Fig. 1.5 B) and reversibly disrupt the actin cytoskeleton when added to cells [56]. Latrunculins do so by binding to glob-

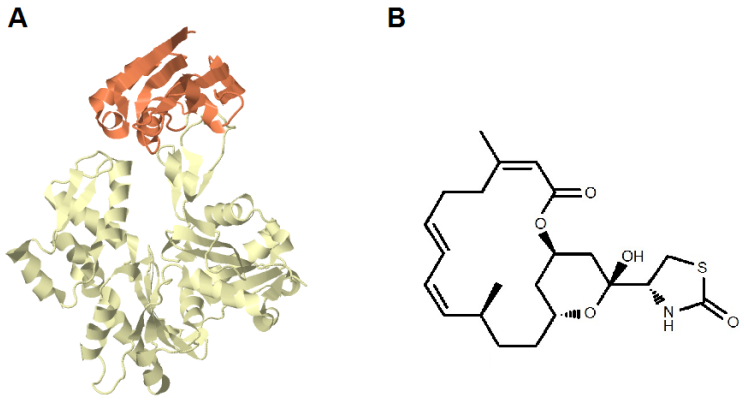

Figure 1.5: **A:** Actin:DNase I complex (PDB: 3W3D) **B:** Structure of Latrunculin A.

ular actin, thus inhibiting the formation of new filaments [57]. Since its discovery, LatA has been used widely as specific actin filament dipolymerizing drug.

LatA binds G-actin above the ATP binding site between subdomains 2 and 4, thereby forming hydrogen bonds to the actin molecule with nearly all of its polar atoms. Binding of the drug does not induce dramatic changes in the actin structure [58]. It is thought to lock ATP in its binding cleft and inhibit the relative rotation of subdomains 2 and 4, which occurs during polymerization [58, 59].

1.2 Fluorescence Spectroscopy

Fluorescence belongs to a series of optical phenomena described with the general term photoluminescence. It referres to the absorbance and subsequent emission of photons. The absorbed photon has a higher energy than the emitted photon, resulting in a shift between absorption and emission spectra called the Stokes shift. The energy difference can be converted to vibrations, heat, or chemical reactions. Quantum mechanically, the phenomenom can be described as an excitation from the ground state S_0, usually in the S_1 state, followed by vibrational relaxation. From the lowest S_1 state, the molecule can relaxate by the emission of a photon (Fig. 1.6).

As an alternative, the molecule can also pass to the triplet state, which is quantum mechanically forbidden and therefore happens with a low rate. The relaxation from

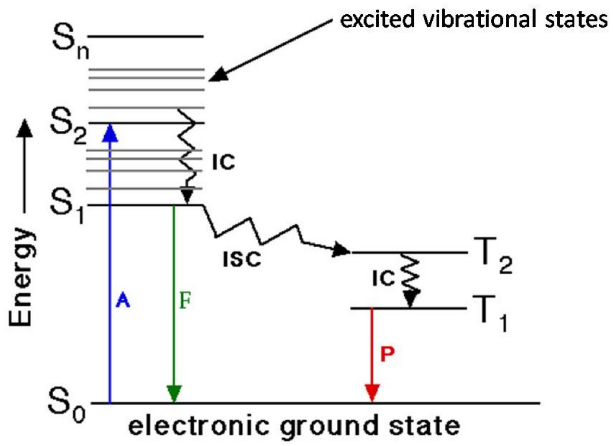

Figure 1.6: **Jablonski diagram.** A: photon absorption, F: fluorescence, P: phosphorescence, S: singlet state, T: triplet state, IC: internal conversion, ISC: intersystem crossing. From [60].

the triplet state under emission of electromagnetic radiation is called phosphorescence.

1.3 Zero-mode waveguides

Zero-mode waveguides allow the *in vitro* investigation of single molecules by fluorescence microscopy at high concentrations by reducing the effective observation volume to the range of 10^{-21} l [8, 61]. They consist of arrays of nanoapertures in metal, i.e. often aluminum, on a glass slide (Fig. 1.7). Fabrication methods start with the evaporation of metal onto the substrate and subsequent etching of defined holes by focused ion-beam milling [62] or electron beam lithography with positive or negative resist [8, 63]. When non-specific binding of biomolecules to the surfaces of the waveguides shall be avoided, the aluminum oxide walls and the silicon dioxide bottom have to be functionalized differently. The aperture walls can be passivated with polyvinyl phosphonic acid, which allows the functionalization of the bottom with neutravidin by physisorption [64].

The name "zero-mode waveguides" derives from the fact that below a certain frequency of light, no propagating modes are allowed inside the waveguide [8]. As the effect occurs for wavelengths longer than 1.7 times the waveguide's diamenter d,

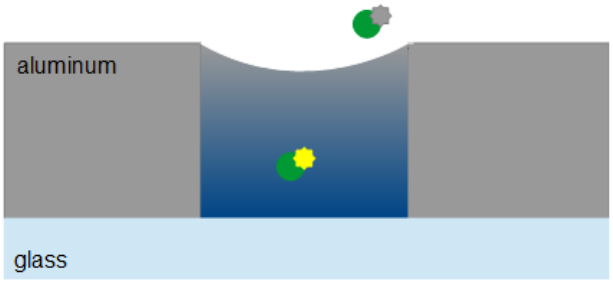

Figure 1.7: **Schematic of a single ZMW.** The small volume (approximately 100 nm in depth and 30 to 300 nm in diameter) allows high ligand concentrations.

only the evanescent field can excite molecules inside the ZMWs in the visible spectrum [65]. The evanescent field stays constant along xy and decays exponentially with Λ in the z-direction:

$$\frac{1}{\Lambda} = 2\sqrt{\frac{1}{\lambda_c^2} - \frac{1}{\lambda_m^2}} \tag{1.1}$$

with the cut-off wavelength λ_c and the wavelength of the light inside the waveguide λ_m [8]. The intensity profile thus follows $e^{-z/\Lambda}$, which sets the observation profile to

$$S(z) = e^{-3z/\Lambda}, \tag{1.2}$$

when the coupling efficiency and the quantum efficiency of the fluorophore are considered to be proportional to the intensity profile [66]. The observation volume then follows to be

$$V_O = \frac{\pi d^2}{4} \frac{(\int S(z)dz)^2}{\int S(z)^2 dz} = \frac{\pi d^2 \Lambda}{24}, \tag{1.3}$$

which allows single-molecule measurements at a concentration of 10 μM for a ZMW with 100 nm diameter and illumination with 488 nm light [65].

The possibility to use high concentrations allows for enzymatic studies on the single-molecule level also for enzymes with Michaelis-Menten constants in the micromolar range, which in fact is the case for most enzymes. Levene et al. for example observed the incorporation of fluorescent nucleotides by the T7 DNA polymerase in real time [8], an approach that has been further delevoped towards parallel DNA

sequencing [67]. Protein-protein interactions can be studied in real time because of the short residence time of the molecules in the observation volume [68]. The restricted volume also allows fluorescence correlation spectroscopy studies using high concentrations of freely diffusing molecules in solution [62, 66, 69], or across lipid membranes [70, 71].

1.4 Step-finding Algorithms

As the signal to noise ratio is rather low in measurements with zero-mode waveguides, it is challenging to detect the stepwise intensity changes that occur when a labeled actin monomer is bound to the tethering protein. For this purpose, several step-finding algorithms have been compared in this thesis.

Step-finding or step-smoothing algorithms seek to remove the noise from piecewise constant signals to reveal the position and height of the underlying steps. There are several approaches to this problem. Some algorithms use sliding windows to break the signal into smaller pieces and evaluate them separately, as for example the running mean or running median filter. For this approach, the result can depend on the selected window size, as the smoothing fails for steps longer than the window size, or the algorithm omits steps if several steps are located in one window [72].

Recursive algorithms work by segmenting or merging constant regions. The Kalafut-Visscher (KV) algorithm represents a top-down approach of recursive methods, starting with a single step fit and subsequently increasing the number of steps [73]. It yields generally good results with a slight tendency towards overfitting for data with independent, Gaussian noise. With correlated noise however, it shows slightly larger errors than other algorithms [74].

Finally, global methods consider the whole time series at once, like for example the L1-trend filter [72].

In the following, the KV algorithm and the L1 filter, as well as a method based on the χ^2 error will be discussed shortly.

1.4.1 Kalafut-Visscher Algorithm

The Kalafut-Visscher algorithm is, unlike other step-finding algorithms, model-independent, so that no parameters have to be defined by the user [73]. It minimizes the Schwarz Information Criterion (SIC, also referred to as Bayesian Information Criterion, BIC) to determine the number and location of steps [75]:

$$SIC = -2\log\mathcal{L}(\hat{\theta}) + p\log n \tag{1.4}$$

with $\mathcal{L}$ the likelihood function of the statistical model, $\hat{\theta}$ the vector of parameters which maximize the likelihood (here, means and variances), p the number of parameters and n the number of data. For the normal distribution $\mathcal{N}$, $\mathcal{L}$ can be derived from the maximum likelihood estimators for the mean $\hat{\mu} = \frac{1}{n}\sum_{i=1}^{n} x_i$ and the variance $\hat{\sigma}^2 = \frac{1}{n}\sum_{i=1}^{n}(x_i - \hat{\mu})^2$:

$$\mathcal{N} = \frac{1}{\sigma\sqrt{2\pi}} e^{-\frac{1}{2}(\frac{x-\mu}{\sigma})^2} \tag{1.5}$$

$$\mathcal{L}(x_1, ..., x_n) = \prod_{i=0}^{k} \prod_{l=j_i}^{j_{i+1}-1} \frac{1}{\hat{\sigma}_{j_1,...,j_k}\sqrt{2\pi}} e^{-\frac{1}{2}(\frac{x_l-\mu_i}{\hat{\sigma}_{j_1,...,j_k}})^2} \tag{1.6}$$

with steps (mean shifts but no variance shifts) at j_1 to j_k ($j_0 = 0$ and $j_{k+1} = n+1$). Substituting $\mathcal{L}$ in eq. 1.4 and neglecting all constant values results in

$$SIC_{j_1,...,j_k} = (k+2)\log n + n\log\hat{\sigma}_{j_1,...,j_k} \tag{1.7}$$

with $p = k + 2$, k is the number of steps.

The SIC is tendentially biased towards underfitting, which for biological studies was favoured over overfitting by the authors. To reduce computational costs, the SIC is not calculated for all possibilities. The algorithm starts with the SICs of fitting the data with no step at all versus the best one-step solution. When one step is favoured over no steps, it continues by comparing this solution to the SIC of a second step fit, thus adding more steps only when the SIC of the previous one has been smaller than the SIC of the fit with less steps.

Because Chistol et al. found inaccaptable overfitting of the KV algorithm applied to steps of a DNA packaging motor measured with optical tweezers, they introduced a penalty factor (PF) for additional steps in the first term of eq 1.7, which they set to 5 for their applications [76].

1.4.2 L1-regularized Global Step-smoothing

The L1-trend filter based algorithm L1-PWC by Max Little et al. as well uses Bayesian methods [72, 74, 77]. The unknown series of positions μ_t is hidden by independent Gaussian noise ϵ_t, such that $\theta_t = \mu_t + \epsilon_t$, θ_t being the observed series of positions. m_t, the smoothed estimate of the underlying positions, is obtained by minimizing the following function over different possible positions m'_t [74]:

$$m_t = \arg\min_{m'_t} \sum_{t=1}^{T} (\theta_t - m'_t)^2 + \lambda \sum_{t=2}^{T} \mid m'_t - m'_{t-1} \mid \tag{1.8}$$

Here, the first term is the error of the estimation, the second term the difference between two subsequent positions, weighted by the λ-factor. To obtain any smoothing, λ has to be greater than zero, otherwise the estimate will exactly follow the observed signal θ. As the underlying series represents a trace of piecewise constant signal with steps in between, the second term will be zero for most t, increasing the probability to find the correct positions of steps.

1.4.3 Step-finding according to Salapaka

Aggarwal et al. developed a step-finding algorithm for single-molecule data based on a cost function calculated using the χ^2 error [78]. When y is the measured signal with the hidden true stepping signal x, the χ^2 error for the estimate $\hat{x}$ at each time point or sample k is $\sum_k (y_k - \hat{x}_k)^2$.

The χ^2 error plus a penalty term for the introduction of false positive steps build

the cost function $J(\hat{x})$:

$$J(\hat{x}) = \sum_{k=1}^{N}(y_k - \hat{x}_k)^2 + W\sum_{k=1}^{N}\delta(\hat{x}_k - \hat{x}_{k-1}) \tag{1.9}$$

with N the total number of samples and $\delta(x) = 0$ for $x = 0$, otherwise $\delta(x) = 1$. W is a penalty factor for the introduction of additional steps and has been set to $9\sigma^2$ by the authors, with σ being the standard deviation of the noise.

1.5 Single-molecule Kinetics and Mechanisms

Traditionally, enzyme kinetics seek to reveal the enzymatic mechanism by looking at the mean rate of product formation. The study of individual molecules, however, has shown that rate fluctuations due to the stochastic nature of thermal activation are an important factor in biologically catalyzed reactions [79–81]. A measure for these fluctuations is the randomness parameter r. As the number and order of the kinetic intermediates with their specific lifetimes have impact on the rate fluctuations of single enzymes, the value of r gives insight into the minimum number of intermediate states, thus restricting the number of possible enzymatic mechanisms [9, 79, 80]. r is defined as the ratio between the variance and the mean squared of a given dwell time distribution:

$$r = \frac{\langle t^2\rangle - \langle t\rangle^2}{\langle t\rangle^2} \tag{1.10}$$

The inverse of the randomness paramater is n_{min}, the minimum number of states of a valid kinetic model, or more appropriate, the effective number of rate-limiting transitions [9]. This relationship between r and n_{min} has been proven for any series of states that can include loops or branching, or multiple visits to one state [82]. The two assumptions made here are that the enzyme under investigation has no memory of how it got to each state and no memory of how long it visited the state.

The randomness parameter can be visualized as the quantifying parameter of the shape of the dwell time distribution (Fig. 1.8). Only for a single-exponential decay,

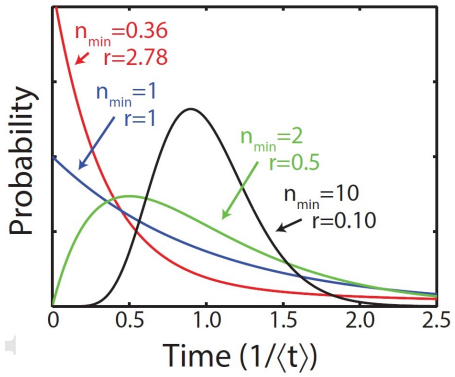

Figure 1.8: **The randomness parameter as a measure for the shape of the dwell time distribution.** Red: multi-exponential decay, blue: single-exponential decay, green: gamma distribution with two states, black: gamma distribution with ten states. From [9].

r and n_{min} are 1. For a gamma distribution, r is less than 1, whereas for a multi-exponential decay, r is larger than 1. Biophysically, an r >1 can be produced by parallel branches or off-pathway states [9, 83, 84].

The randomness parameter can depend on substrate concentration, when different events become rate-limiting depending on concentration. For example, Moffitt et al. studied the dwell time distributions of the DNA packaging motor of the bacteriophage ϕ29, which consists of a homomeric ring of ATPases [85]. They observed a dependency of n_{min} on ATP-concentrations, with a value >1 for very low ATP-concentrations, indicating that more than one ATP is bound to the motor per cycle. Additionally, n_{min} is >3 for saturating ATP-concentrations, which lead to a model with at least four kinetic states per cycle [86].

1.6 Objectives

The goal of this thesis is to elucidate the kinetics and mechanisms of actin nucleation by directly measuring the arrival times of the individual actin monomers that form the new filament *in vitro*. The high concentrations needed for actin assembly can be measured using the confined small observation volume of zero-mode waveguides. With different biotinylated actin-binding proteins at the bottom of the single waveguides, barbed end elongation and pointed end elongation can be studied separately.

Using nearly 100% fluorescently labeled actin, the individual arrival times can be determined in the measured intensity traces over time. By determining the rates of the individual monomers at different concentrations, their rate constants can be designated.

The high statistics of each measurement due to the array structure of the waveguides makes it possible to gain additional information from the shape of the arrival time histograms. The randomness parameter as the variance over the squared mean of the distribution is directly associated to the minimum number of underlying kinetic states.

Bound to Latrunculin A, actin is trapped in the ATP-bound conformation. Besides, it is assumed that the flattening is hindered that occurs during the structural transition from monomeric to filamentous actin. The effect of this drug on the number and arrival time distributions of the individual steps gives insight into the timepoints of ATP hydrolysis and flattening.

2 Materials and Methods

2.1 Wide-Field Microscopy Set-up

Measurements were performed with a 60x oil objective (Nikon Apo TIRF series, numerical aperture 1.49, Nikon Instruments Inc, Melville, USA) at 23°C. Laser power was adjusted to be 5 mW for 488 nm and 561 nm after the fiber into which the laser light is coupled, of which approximately 50% are guided into the microscope.

The exposure time was set to be 100 ms, with varying cycle times from 150 ms to 500 ms.

2.2 Sample Preparation

2.2.1 Actin Nucleation Assays

All proteins were stored at -80°C and kept on ice during the measurement day.

The ZMWs (Pacific Biosciences, Menlo Park, Canada) were incubated with 20 μl 0.33 mg/ml Streptavidin in phosphate buffered saline (PBS) buffer (137 mM NaCl, 2.7 mM KCl, 10.1 mM Na_2HPO_2 dihydrate, 1.75 mM KH_2PO_4, pH 7.0) for 5 min. After washing with 30 μl PBS, 30 μl of the biotinylated tethering protein was added (Actin, Gelsolin or DNase I-atto594, freshly diluted in G-buffer to 200 nM). After incubation for 5 min and washing with 30 μl G-buffer (5 mM Tris pH 7.8, 0.1 mM $CaCl_2$, 0.2 mM ATP, 1 mM Dithiothreitol, stored at 4°C), 10 μl G-buffer was added to the array to avoid drying out.

100 % labeled rabbit skeletal muscle actin-atto488 (Hypermol, Bielefeld, Germany, stored at -80°C), diluted in G-buffer, was incubated in an exchange buffer for 5 min on ice (ME buffer, 50 μM $MgCl_2$, 0.2 mM EGTA). Latrunculin A or Profilin were

added to actin after 4 min. on ice and incubated for 1 min. Latrunculin A was used at 10x actin concentration, Profilin at 4x.

Parallely, a polymerization buffer (KMEI buffer, 50 mM KCl, 1 mM $MgCl_2$, 1 mM EGTA, 10 mM imidazole HCl at pH 7.0) was mixed with photococktail (2.5 mM protocatechuic acid (PCA), 250 nM protocatechuate-3,4-dioxygenase (PCD) and 1 nM Trolox) [87, 88]. In case of gelsolin as tethering protein, instead of KMEI, KMC buffer was used. ME, KMEI and KMC buffer were stored as 10x buffers at room temperature.

After starting polymerization by mixing the polymerization buffer and the actin (final volume 80 μl), 40 μl were added onto the waveguides and data acquisition was started immediately. For the analysis, time 0 was defined as the timepoint of adding the actin in polymerization buffer onto the waveguide. Per independent measurement, about 700 traces have been analyzed.

2.2.2 DNA Measurements

50 μl 100 nM DNA, labeled with 4, 6 or 8 atto488 dyes in PBS were added to the waveguides after streptavidin incubation as described above. After incubation for 30 min and washing, acquisition was started at 5 mW or 20 mW laser power with or without photococktail.

2.3 Analysis

The background-corrected traces of each intensity peak have been analyzed with the step-finding algorithm by Salapaka et al. using a penalty factor of 50 [78]. At higher concentrations, it is possible that the kinetics get too fast to be resolved well by the algorithm. When too many steps are missed, the step size distribution changes. Therefore, when in an individual trace the mode of the step sizes in that trace is larger than the mean, its value is halfed. When then an individual step is larger than 1.5 times the mode, but smaller than 2.5 times the value, two steps are

assumed. When it is larger than 2.5 times the halfed mode value, three steps are assumed. The missed steps are then given a waiting time equal to the imaging cycle time. For this reason, for the second step onwards the first bin in the waiting time distribution is very high and therefore is not considered for further analysis.

The found steps are sorted into the first step in a trace, the second, etc. up to the sixth step. Only upward steps before the first downward step are sorted in these defined steps. After the first downward step, all upward steps are pooled in polymerization steps, and all downward stes are pooled in depolymerization steps. Additionally, the dwell time of the first downward step is determined with respect to the beginning of the measurement. The dwell time for every other downward step is determined with respect to the timepoint of the previous step. The arrival times for the first six steps, as well as the polymerization and depolymerization steps are fitted with either an exponential decay or a gamma distribution. When the difference of the Bayesian information criterion for the gamma fit and the exponential fit is larger than two, the gamma fit is applied. Otherwise, an exponential decay is used to fit the data. When the gamma distribution is used, the rate k as well as the number of underlying kinetic intermediates n is fitted according to $\cdot k^n \cdot x^{n-1} \cdot e^{-kx} \cdot \Gamma(n)^{-1}$. Apart from the fit, the randomness parameter r and n_{min} are calculated from the variance and the mean of the data.

Analysis and simulations have been performed in Matlab^{TM} 2014a.

3 Results

3.1 Comparison of Step-finding-algorithms

For the testing of step finding algorithms, the polymerization of monomers has been simulated for 10,000 traces with a time stepping of 0.1 s (Fig. 3.2 B). The on-rates are 0.03 s^{-1} for the addition of the first two monomers, 0.05 s^{-1} for the third monomer and 0.01 s^{-1} for onward polymerization. The off-rate is held constant at 0.004 s^{-1}. The addition of a monomer results in a step upwards, such that the size of each step is 1. When six monomers arrived, the trace is ended after a fixed prolongation at the same value. White gaussian noise is added to the trace with a signal to noise ratio (SNR) of 1.

Three approaches have been tested, the algorithms by Kalafut-Visscher (KV), by Salapaka and a combined algorithm of L1 and KV, which are described in the theory section. Parameters of interest are the number of steps the respective algorithm finds in comparison to the true number of steps, the rates of the addition of monomers, and the randomness parameter r of the found dwell time distributions. As no multiple states of the monomers or cooperativity were simulated, r should always be one.

Additionally, measurements of dsDNA labeled with 4, 6 or 8 atto 488 dyes have been performed on zero-mode waveguides to test the ability of the algorithms to find the expected number of steps in a trace hidden by non-gaussian noise, the same conditions as for the measurements of actin nucleation.

For the estimation of the on-rates, steps have been sorted according to step 0 to 1, 1 to 2 etc. Only onward steps before the first found down steps are considered for the arrival time distribution to reduce false sorting of the steps due to spurious downward steps. Down steps are pooled for the distribution to be comparable with the analysis of actin data.

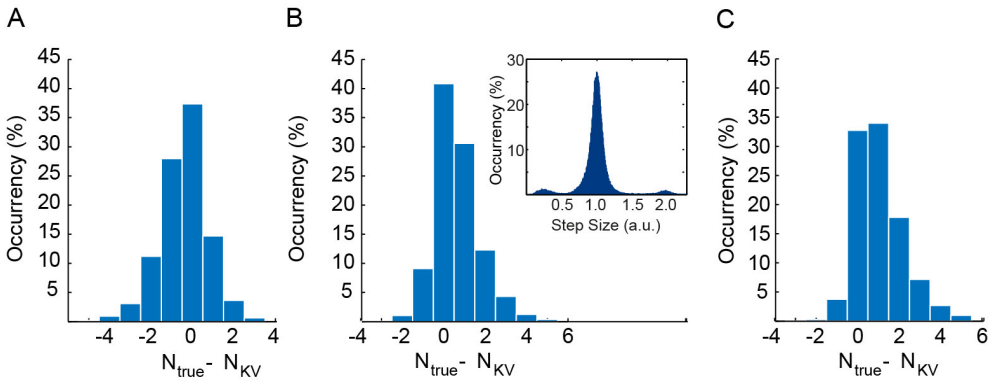

Figure 3.1: **Step finding performance of the KV algorithm.** $N_{true} - N_{KV}$ is the difference between the true number of steps and the number of steps found in the noise-overlayed signal. **A**: PF = 1, **B**: PF = 2, **C**: PF = 3.

3.1.1 Kalafut-Visscher

For the Kalafut-Visscher algorithm, a penalty factor has been introduced [76]. The algorithm has been tested with different penalty factors on simulations (Fig. 3.1). A penalty factor of 1 has no effect on the original algorithm, which finds more steps than are truly hidden in the noise (Fig. 3.1 A). With a penalty factor of 2, the correct number of steps is found in approximately 41% of the traces, whereas with a penalty factor of 3, the whole distribution gets shifted to higher values, i.e. the number of found steps is lower than the correct number of simulated steps.

With a penalty factor of 2, the step size of the found steps is mostly around 1, as simulated, with two minor peaks at 0.25 and 2.0. The on- and off-rates of simulated data are recovered with small deviations (table 3.1). All rates are derived from an exponential fit of the waiting time distribution. The addition of the first monomer is estimated rather too low, whereas the recovery of the slow on-rates of steps 3 to 6 gives slightly higher values (0.013 s^{-1} vs. 0.01 s^{-1}). The rate of the fastest step (0.05 s^{-1}) is recovered well, however, the randomness parameter of the dwell time distribution has a value of 2.3. For the off-rate of the pooled down steps, r is close to 1, however, the rate is estimated far too high (0.017 s^{-1} instead of 0.004 s^{-1}).

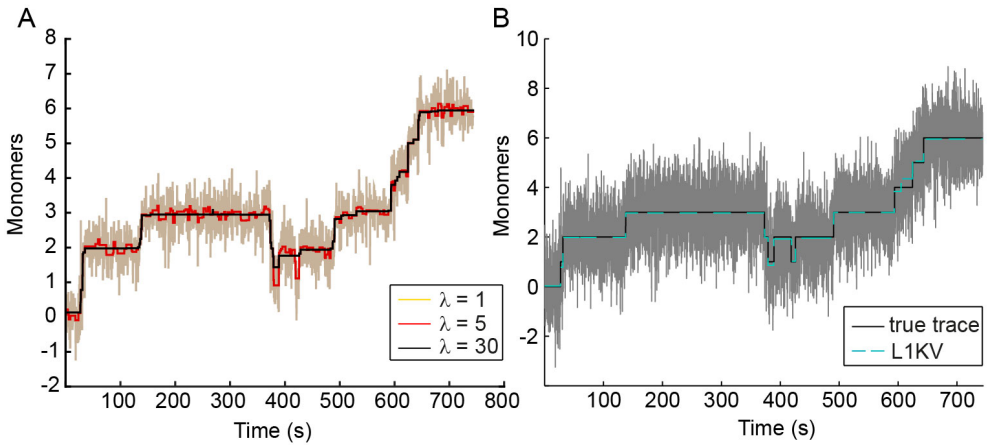

Figure 3.2: **The L1KV algorithm. A:** Effect of the parameter λ. Higher values increase the smoothing, which can lead to the suppression of fast transitions. **B:** Simulated example trace (black line) with added noise (grey) and the recovered trace by the L1KV algorithm (blue dashed line).

3.1.2 L1KV

The KV algorithm has been shown to be less reliable with correlated noise [74]. Therefore, the L1KV algorithm was developed by using the L1 algorithm by Max Little et al. [72] to smooth the trace prior to the actual step-finding by the KV algorithm with a high penalty factor. Different combinations of the paramters λ in the L1 and PF in the KV algorithm have been evaluated (for the description of the parameters, see theory section). Increasing λ augments the smoothing effect, but can go to the cost of loosing fast transitions during the process (Fig. 3.2 A). Different combinations of λ and PF have been evaluated. Because of the best finding of the correct rates in simulated data, the combined algorithm was set to $\lambda = 1$ and PF $= 5$.

With these settings, the L1KV algorithm recovers the correct number of steps +/- 1 in most cases, with a slight tendency towards overfitting (Fig. 3.3 A). Most of the steps are assigned correctly to a step size of 1, however, some of the found steps show heights below 0.5.

As the Kalafut-Visscher algorithm alone, the L1KV is able to recover the rates of simulated data within a small error range (table 3.1). The arrival times for the first and second monomers are recovered very well. The fastest on-rate is slightly

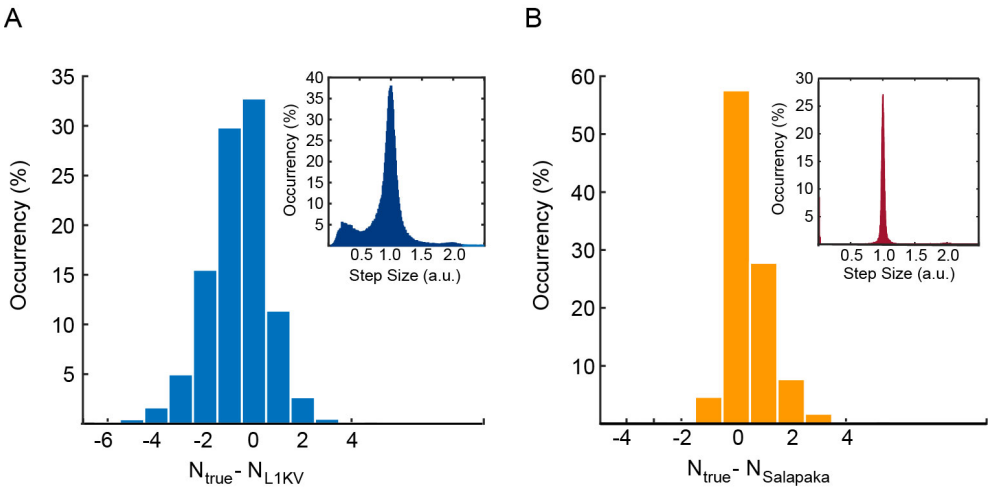

Figure 3.3: **Recovery of the number of simulated steps. A:** L1KV algorithm, **B:** Salapaka algorithm. Insets: Step size distribution of both methods.

Table 3.1: **Performance of L1KV and Salapaka on simulated data.** The on- and off-rates are determined via an exponential fit of the dwell time distribution. k_{off} is the pooled rate of all found downward steps. r is the randomness parameter of the dwell time distribution.

Step	true	KV (PF = 2)		L1KV (PF = 5)		Salapaka (PF = 50)	
	rate (s^{-1})	rate (s^{-1})	r	rate (s^{-1})	r	rate (s^{-1})	r
0 to 1	0.03	0.025	0.9	0.031	1.0	0.026	0.9
1 to 2	0.03	0.030	0.9	0.032	1.0	0.030	0.9
2 to 3	0.05	0.048	2.3	0.059	2.4	0.046	2.0
3 to 4	0.01	0.013	1.1	0.019	1.4	0.012	1.0
4 to 5	0.01	0.013	1.0	0.015	1.2	0.013	0.9
5 to 6	0.01	0.014	1.1	0.014	1.2	0.014	0.9
k_{off}	0.004	0.017	1.1	0.026	1.5	0.015	0.9

overestimated, and the randomness parameter is too high (2.4). The on-rates of the subsequent steps are determined too be faster than the true rates. However, the error gets smaller with the addition of more monomers. The off-rate of all down steps pooled together is estimated too high by a factor of almost 7.

The L1KV algorithm applied to the DNA bleaching traces finds on average 4 and 6 bleaching steps for DNA strands with four and six dyes, respectively (table 3.2). For DNA labeled with 8 dyes, 5 to 6 bleaching steps have been found.

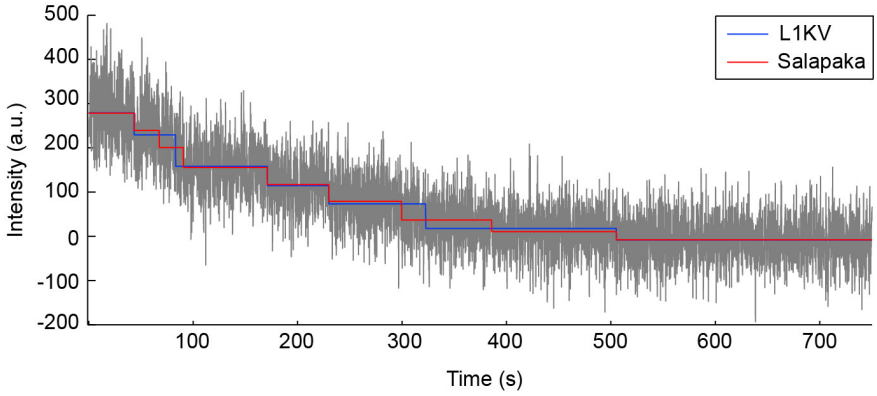

Figure 3.4: **Bleaching of a DNA strand with 8 dyes.** Grey: measured trace, blue: trace found by the L1KV algorithm, red: trace found by the Salapaka algorithm (PF = 50).

3.1.3 Salapaka

The Salapaka algorithm is the only one of the tested approaches that considers the step size distribution to find the step positions. Like for the Kalafut-Visscher algorithm, a penalty factor PF for the introduction of additional steps can be set. The authors set the penalty factor to nine, however, the best factor for measurements with waveguides can be different. Bleaching experiments of biotinylated DNA strands labeled with 4, 6 or 8 dyes (atto488) in waveguides have been analyzed for this purpose, amongst others (Fig. 3.4).

Increasing the penalty factor results in a decrease of the number of very fast transitions (Fig. 3.5 A). Since the number of various longer steps increases simultaneously, the omitted fast transitions are likely to be fast forward-backward steps, thus in a bleaching experiment mostly spurious steps. Supporting this assumption, the number of upwards steps is relatively high at a PF of 9, at higher penalty factors however, no upwards steps are found in almost all traces.

The changes in the waiting time distribution are reflected by the randomness parameter r (Fig. 3.5 B). At high PF however, r reaches a constant region, as do the number of found steps and the bleaching rates (Fig. 3.6). According to these findings, the penalty factor for the Salapaka algorithm was set to 50 for all further analysis.

The algorithm with a penalty factor of 50 finds the correct number of steps in almost

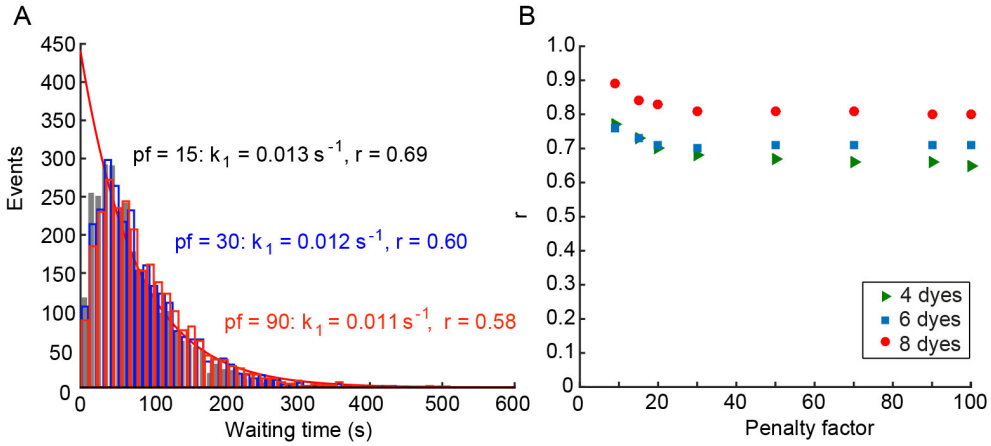

Figure 3.5: **Changing the penalty factor. A:** Waiting time distribution for all bleaching steps of DNA strands with four dyes for three different penalty factors PF_S (n = 512). Red line: exponential fit for PF = 15. **B:** Randomness parameter r vs. the penalty factor for DNA strands with 4, 6 or 8 dyes (n_4 = 1549, n_6 = 2182, n_8 = 738).

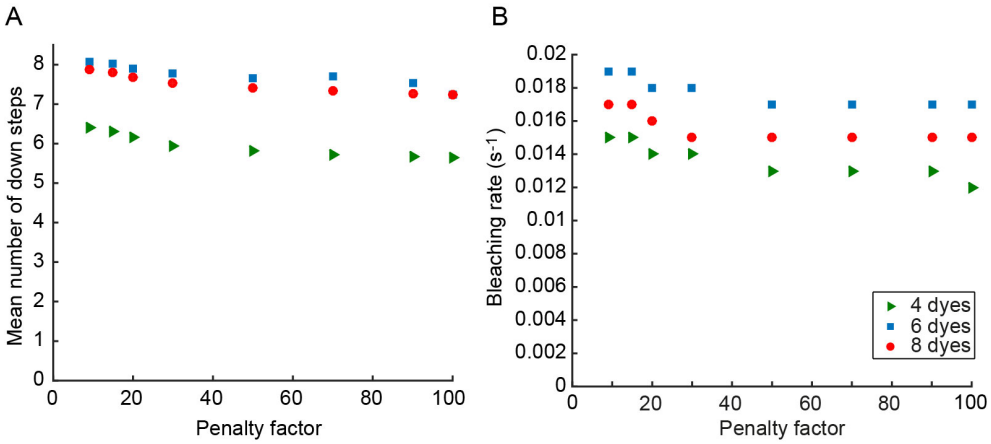

Figure 3.6: **Changing the penalty factor. A:** Mean number of bleaching steps of labeled DNA strands. **B:** Rates of all bleaching steps determined from an exponential fit (n_4 = 1549, n_6 = 2182, n_8 = 738).

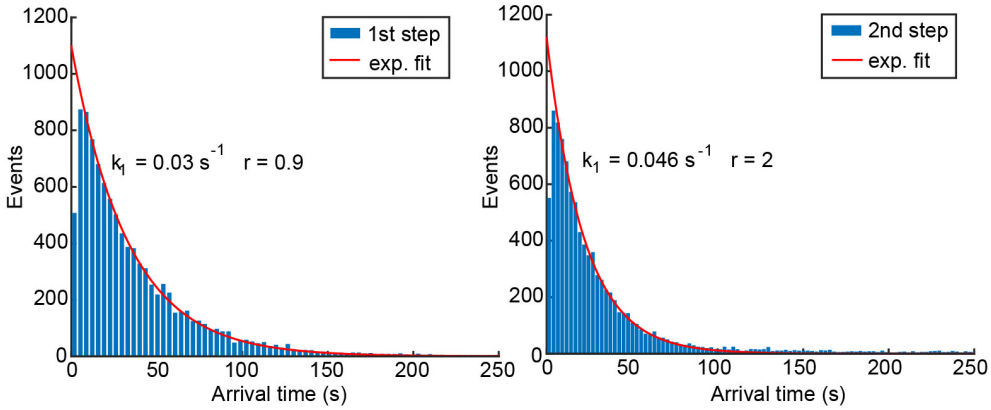

Figure 3.7: **Arrival time distributions. A:** Arrival times of the second monomer (simulated rate 0.03 s^{-1}), **B:** Arrival times of the third monomer (simulated rate 0.05 s^{-1}). Red lines: exponential fit. Salapaka algorithm, $PF_S = 50$.

60% of the simulated traces (Fig 3.3 B). The distribution shows a slight tendency towards underfitting, however, the number of steps found by the algorithm differs little from the true number of steps in both directions (under- and overfitting). The found step size is around one for almost all steps (Fig 3.3 B, inset).

The rates according to an exponential fit of the waiting time distribution are recovered similarly to the other algorithms. The slow rates are overestimated slightly, whereas the arrival times of the first two steps are recovered well (table 3.1, Fig. 3.7). The fastest rate is estimated correctly, however, the randomness parameter is too high.

Applied to DNA bleaching experiments, the Salapaka algorithm assignes tendentially too many steps for the four-dye labeled DNA, whereas for the DNA with six dyes, most traces are fitted to the correct number of steps (table 3.2). For DNA with eight dyes, the algorithm found six bleaching steps.

3.1.4 L1KV and Salapaka applied to Actin Polymerization

During evaluation of actin polymerization measurements, a dependence of the step sizes on actin concentration was observed (Fig. 3.8). Whereas the L1KV algorithm merely shifts the distribution to larger values, the Salapaka algorithm assigns steps with around the same sizes as at the lower concentration and additional larger steps,

Table 3.2: **Performance of L1KV and Salapaka on labeled DNA.** The mean number of down steps found by each algorithm, the determined bleaching rate from an exponential fit and the mean of the step size distribution are compared. The maximum of the step distribution is shown in brackets. ($n_4 = 1549$, $n_6 = 2182$, $n_8 = 738$).

Dyes	Down steps		Rates (s^{-1})		Step size (a.u.)	
	L1KV	Salapaka	L1KV	Salapaka	L1KV	Salapaka
4	4.3 (3)	5.8 (5)	0.010	0.013	30.2	38.6
6	6.2 (6)	7.7 (6)	0.011	0.017	33.1	41.5
8	5.2 (6)	7.3 (6)	0.037	0.015	36.0	37.1

leading to a second peak in the size distribution. The distribution of the mean step size per single trace shows a homogenous distribution, indicating that both step sizes can occur in the same trace, rather than being split into brighter and less bright traces. As the second peak in the size distribution of higher actin concentrations is at approximately twice the value of the peak at lower concentrations, those steps are thought to be double steps.

Using a method to identify double-or triple steps based on the relation between the mode and the mean of the step size distribution (see section "Analysis"), the step size of the assigned multiple steps can be corrected by division by 2 or 3, respectively. This correction results in the reduction of the peak at higher size values to a mere shoulder (Fig. 3.9 A). The number of upward steps increases for some traces, as each double step is counted as two steps, however, the number of total upward steps (after substraction of downward steps) is not affected as much (Fig. 3.9 B, C, table 3.3).

The double step correction does not have a big effect on the determined rates (table 3.3), only the rates of the higher steps increase slightly. Compared to the L1KV, the Salapaka algorithm determines higher on- rates, especially for the first steps. The number of steps upwards and downwards differs by a factor of more than 2 between L1KV and Salapaka, however, the total number of upward steps in a trace is determined similarly by both algorithms. The mean step size varies as well. Only the Salapaka algorithm with double step correction yields a mean step size around 40, similar to those of the DNA bleaching measurements (table 3.2).

Overall similar results are achieved in terms of the randomness parameter and the fitted number of states per step n (table 3.4). For fitted kinetic intermediates of

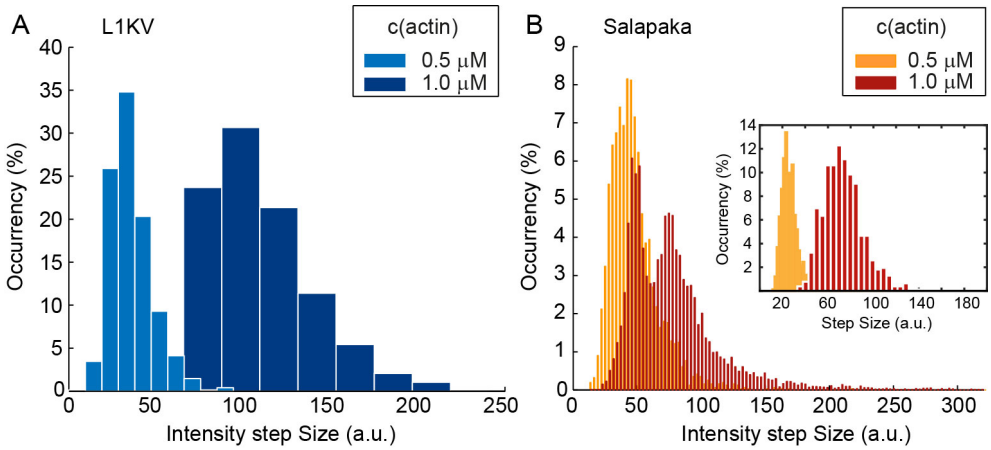

Figure 3.8: **Step size distribution changes with actin concentration. A:** L1KV algorithm, **B:** Salapaka algorithm. Inset: Distribution of the mean step size per single trace. 200 nM Gelsolin were used as tethering protein.

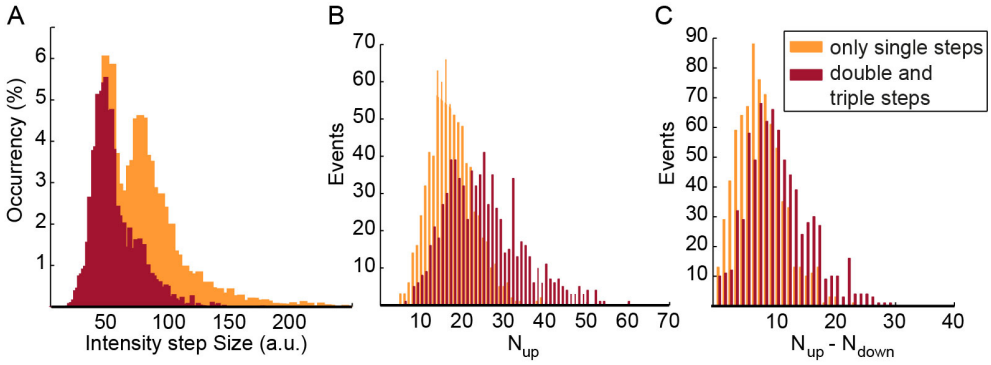

Figure 3.9: **Effect of double step correction. A:** Step size distributions of 1 μM actin with and without double step correction, **B:** Mean number of upward steps N_{up}, **C:** Mean number of upward steps after substraction of downward steps.

Table 3.3: **L1KV and Salapaka with and without double step correction.** Given are rates for the first 4 steps, the mean number of steps upwards, downwards, and the total upwards steps in a trace as well as the mean step size determined for 1 μM actin on 200 nM gelsolin as tethering protein.

	rates (s^{-1})				number of steps			step size
	0t1	1t2	2t3	3t4	up	down	total up	(a.u.)
L1KV	0.28	0.09	0.04	0.02	8.7	3.9	4.8	73.2
Sal	0.73	0.15	0.09	0.06	21	14	6.3	61.3
Sal-ds	0.74	0.16	0.13	0.08	29	18	9.3	43.1

Table 3.4: **L1KV and Salapaka.** Comparison of the randomness parameters and fitted n, determined for 1 μM actin on 200 nM gelsolin as tethering protein.

	r				n			
	0t1	1t2	2t3	3t4	0t1	1t2	2t3	3t4
L1KV	0.24	0.93	0.75	0.68	5.0	2.7	1.7	1.2
Sal	0.17	0.64	0.62	0.74	9.3	2.5	2.0	1.7
Sal-ds	0.22	0.63	0.72	0.70	9.3	2.5	2.0	1.9

the first step, the largest deviations between the L1KV (n = 5), and the Salapaka algorithm (n = 9). However, the subsequent steps are in good agreement.

3.1.5 Discussion

On simulated data, differences between the tested algorithms can be seen mainly in the step size distributions of the found steps. Only the Salapaka algorithm is able to recover the step size of 1, the L1KV and the KV find also lower steps with a size less than 0.5 (Fig. 3.3, 3.1). The KV seems to omit steps, leading to a peak in the size distribution at 2. Accordingly, the Salapaka algorithm finds in almost 60% of the traces the correct number of steps, compared to almost 35% by the L1KV and about 40% by the KV algorithm.

The rates are recovered well by all three algorithms. The L1KV finds the arrival times of the first monomer best, the KV and the Salapaka tend to undererstimate the rate only by 15 or 12%, respectively. All algorithms recover the fastest rate tested (0.05 s^{-1}), however, the waiting time distribution is characterized by all algorithms by a randomness parameter of 2. The distribution is still well fitted by a mono-exponential decay (Fig. 3.7). The reason for the high r value is therefore rather found in the very long waiting times, which are the result of missed steps. Simulations with the fastest rate at the first or second position instead have been analyzed. At the second position, recovered rates and r values show no difference to the results presented here, at the first position however, the rate and the randomness parameter are recovered both well (Appendix III).

The waiting time distributions show lower populations than expected in the first time bins (Fig. 3.7), as the very fast steps are more likely to be omitted by the

step-finding algorithms. However, this has a rather small effect on the randomness parameter (table 3.1).

Slow rates ($0.01\ ^{-1}$) are generally overestimated by about 30% by all step-finding approaches, but least so by the Salapaka algorithm (20% overestimation). The downward steps were simulated with the slowest rate ($0.004\ ^{-1}$), which seems to be nonresolvable, as the downward rate is estimated far too fast by every tested algorithm.

Generally, the simulations show a good capability of the algorithms to estimate the number of steps in a trace within deviations of generally one or two steps and a good estimate of rates in a range not faster than approximately half of the time stepping (0.1 s), and not slower than about a tenth of the stepping.

The evaluation of the DNA bleaching experiments shows that the tested algorithms are able to give an estimate of the number of steps in a trace with the same noise as the actin measurements will have (table 3.2). DNA labeled with four dyes leads to an estimate of 3 to 5 bleaching steps by the L1KV or the Salapaka algorithm, respectively. DNA with 6 dyes is recovered well by both algorithms, whereas the number bleaching steps of DNA with 8 dyes is underestimated. The reason could either be that the limits of the algorithms are reached and more than six or seven steps can not be resolved, or that over the time some dyes detached from the DNA strands. Interesting would be to measure the DNA strands with a total internal reflection set-up to with higher SNR ratio as a control.

With higher penalty factors, the Salapaka algorithm determines less numbers of steps, slower rates and smaller randomness parameters (Fig. 3.5, 3.6). However, in each case a constant region is reached at PF = 30 to 50. For that reason, the penalty factor was chosen to be 50 for the evaluation of actin data.

The randomness parameter is with 0.85 to 0.65 below the expected value of 1 for an exponential decay too low, because very fast steps can not be resolved, which results in an underpopulation of the first time bins of the waiting time distribution (Fig. 3.5 A).

The determined bleaching rates differ slightly between DNA strands with different

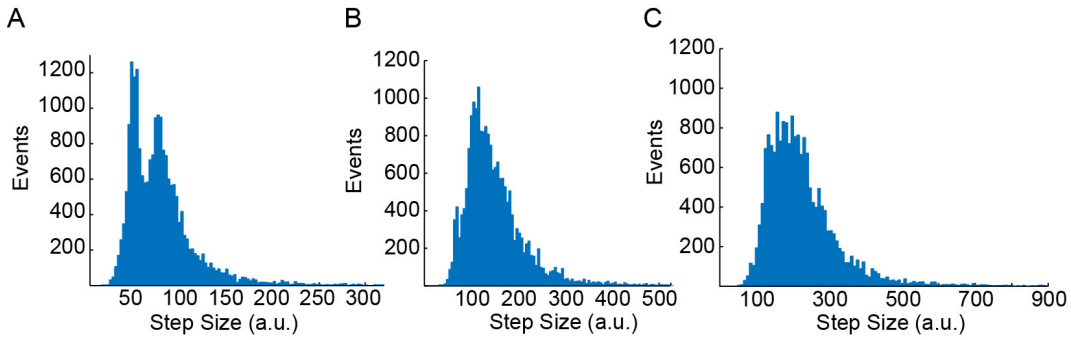

Figure 3.10: **Lowering time resolution.** Step size distribution of 1 μM actin on 200 nM gelsolin. **A:** Original data, measurement rate 0.2 s, **B:** Intensity of 2 subsequent frames summed up to one frame, **C:** Intensity of 3 subsequent frames summed up to one frame. Salapaka algorithm, PF = 50, no double step correction.

number of dyes. However, the rates are very small (0.01 to 0.02 as determined by the Salapaka algorithm with a measurement rate of 0.15 s), which reaches the limits of resolvable rates as the simulations showed. The step sizes of the bleaching steps are similar to those measured at low actin concentrations, indicating a good reproducibility of step sizes in different measurements.

On actin data evaluated with the L1KV algorithm, the step size increases with higher actin concentrations (Fig. 3.8). The Salapaka algorithm shows an increase in the mean step size per trace as well, however, the distribution of the single sizes shows two peaks, which makes an assignment of a step into single- or double steps possible. A double step could either be the result of double labeling, of two monomers arriving too fast after another to be resolved, or the addition of dimers. To estimate the effect of time resolution versus S/N ratio, for a measurement of 1 μM actin with 200 nM gelsolin as tethering protein the intensity of two or three subsequent frames has been summed up, so that the time resolution is reduced, but the SNR ratio is enhanced (Fig. 3.10). The step size distribution as determined by the Salapaka algorithm without double step correction gets shifted towards much higher values. The peak around 50 is completely lost in the processed data, the second peak around 80 is only seen as a minor peak in the doubled intensity version, and disappears in the tripled intensity version. With the doubled intensity, the major step size peak is around 150, indicating that mainly triple steps are found. When time resolution is lowered

further, the main peak gets shifted to around 200, which would correspond to 4 steps seen as one step by the algorithm. These findings indicate that double steps found at the time resolution of the measurement are mainly subsequent monomers that arrive too fast to be resolved. Therefore, the step size distribution of actin data at higher concentrations should be monitored carefully.

Other than to simulated data, the algorithms applied to real data differ in the number of found steps, as well as in the determined rates (table 3.3, 3.4). The Salapaka algorithm finds more steps than the L1KV, especially with double step correction. The difference between the algorithms is more pronounced with actin data than with the DNA measurements, as the Salapaka tends to find more up and down steps than the L1KV, which has more effect on the result in a dynamic trace with upward and downward steps than in a bleaching trace. The Salapaka algorithm with double step correction finds more steps than the L1KV by a factor of 2 to 3, however, it is the only method to yield a step size distribution of around 40, like the DNA measurements and measurements with low actin concentrations. Therefore, the higher number of steps is more consistent in that sense.

Accordingly, the Salapaka algorithm determines higher rates than the L1KV, above all for the addition of the first actin monomer. The number of underlying kinetic intermediates, however, is determined similarly by all methods, only the first step shows some deviation between Salapaka and L1KV.

Overall, the Salapaka algorithm determines more dynamics, with more steps and faster rates than the L1KV algorithm. The simulations showed a good capability of the algorithms to recover the number of steps and the rates of traces hidden in white noise. Applied to real measurements, the differences between the algorithms become more pronounced. However, slow rates like that of the DNA bleaching could be recovered with minor deviations from different measurements. With the Salapaka algorithm, it is possible to correct for missed steps, as long as the time resolution is sufficiently high. This can be monitored via the step size distribution. With a SNR of 1, approximately 40 measurement points per step are necessary for the Salapaka algorithm to identify it [78].

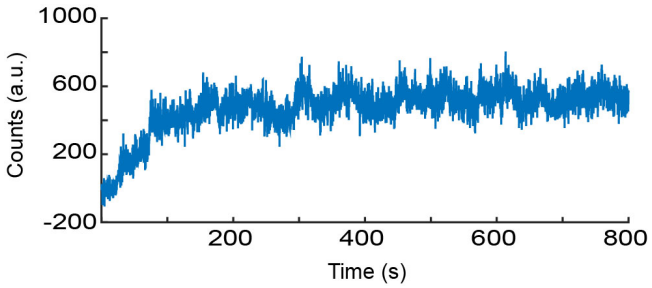

Figure 3.11: **Example trace.** 1.75 μM actin on 200 nM gelsolin

3.2 Gelsolin-mediated Pointed-end Filament Nucleation

With 200 nM biotinylated gelsolin as tethering protein, actin concentrations ranging from 350 nM to 2 μM have been measured. Images have been mostly taken every 200 ms, with an exposure time of 100 ms and at a total measurement time of 800 s. The lowest concentration has been imaged every 0.5 s with1500 s measurement time in total. Traces have been analyzed with the Salapaka algorithm as described in the analysis section. A representative example trace for 1 μM actin concentration is shown in Fig. 3.11. After a steep initial increase of the intensity, most traces reach a plateau region. Although the trace does not grow overall in this region, it stays dynamic as a lot of upward and downward steps are detected. Afterwards, some traces show a further increase in intensity, whereas others decrease.

To account for these different stages of a trace, the determined steps have been sorted in four types: the upward steps before the first down step (initial increase), all upward and all downward steps in the whole trace, and the netto number of upward steps in a trace after substraction of the downward steps.

For 1 μM actin, in average 6 monomers are incorporated before the first downward step occured (Fig. 3.12). A small number of traces do not reach a plateau, but increase continuitively, as the number of first upward steps reaches up to 20, and some traces show no or very little downward steps. For most traces, however, about 20 downward steps have been determined. With in average about 30 upward steps, traces are quite dynamic. At 1 μM, mostly about 10 actin monomers are incorporated after 13 min. Some traces show very little or no growth, whereas others seem to grow to larger filaments.

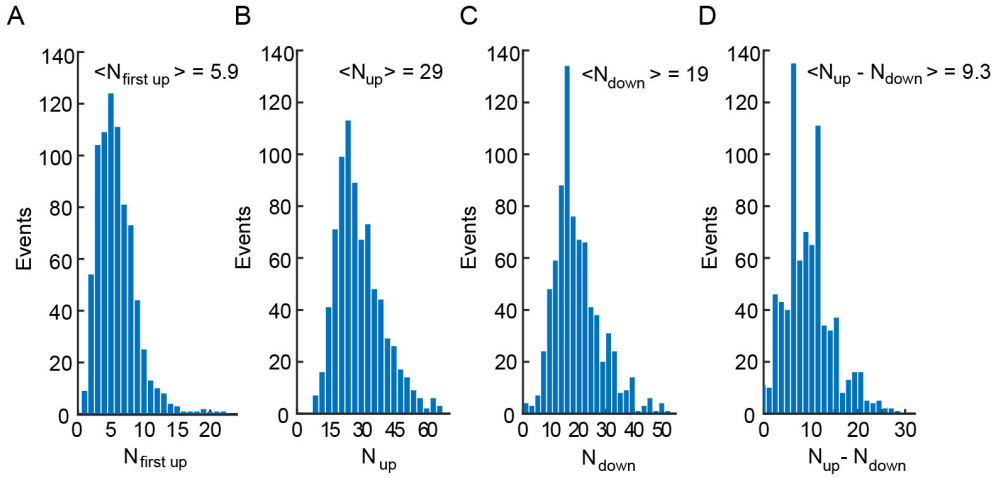

Figure 3.12: **Number of steps for 1 μM actin concentration. A:** Initial increase before first downward step, **B:** Upward steps, **C:** Downward steps, **D:** Number of actin monomers at the end of the measurement (13 min). Mean values are displayed above the histograms. n = 780.

Additionally to the number of steps, the arrival times of the first to the sixth monomer have been determined. For the arrival time distribution, only steps before the first downward step have been considered, first because the downward steps can be either depolymerization or a bleaching event, and second, to prevent too many mistakes in the attribution of steps as first, second, etc. by the step-finding algorithm. After the first downward step, the arrival times of all upward and downward steps are pooled into a distribution for polymerization or depolymerization, respectively. The arrival time distribution was fitted with an exponential or a gamma fit according to the BIC for each fit (see analysis section). For the second step onwards, the first bin of the histograms is not considered for the fit, nor for the calculation of the mean arrival time or the randomness parameter. When double step correction is applied, this bin is very high (Fig. 3.13), because the arrival time for the assumed additional step is considered to be equal to the imaging rate (mostly 1 image in 0.2 s).

The fitted rates are higher than the inverse of the mean arrival times (table 3.5), because the fit considers the number of kinetic intermediates . For the same reason, the first step seems to be faster than the subsequent ones as for the first step, the highest number of kinetic intermediates is found. The mean dwell times at 1 μM

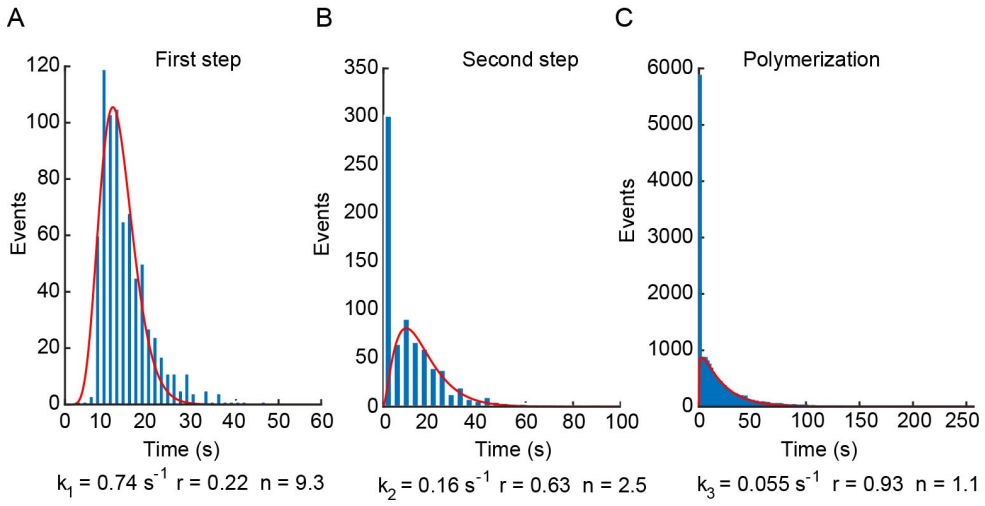

Figure 3.13: **Monomer arrival times for 1 μM actin concentration. A:** First step, **B:** Second step, **C:** Pooled polymerization after the first downward step. Red line: gamma fit. The fitted rates k, the fitted number of kinetic intermediates n, and the randomness parameter r are displayed. The high number of events in the first bins in B and C derives from the correction of double steps and has not been considered in the fit. $n_1 = 746$, $n_2 = 737$, $n_{poly} = 18134$.

Table 3.5: **Mean dwell times and fitted rates k for 1 μM actin.** k and n derive from a gamma fit of the arrival time distribution.

Step	Dwell time (s)	1/Dwell time (s^{-1})	k (s^{-1})	n
1	14.3	0.07	0.74	9.3
2	18.4	0.05	0.16	2.5
3	23.8	0.04	0.14	2.5
4	29.2	0.03	0.08	2.0
Poly	24.5	0.04	0.06	1.1

actin concentration are around 20 s, which means that in average for every intensity step, 100 images have been taken.

In the measured concentration range, the number of upward steps in the initial intensity increase of the traces increases linearly with actin concentration, until at 1.5 μM a plateau seems to be reached (Fig. 3.14 A). The netto number of upward steps at the end of the traces differ only slightly from the initial increase. At low concentrations, the values are slightly lower than those of the initial upward steps, whereas at high concentrations, the numbers tend to be higher. The mean numbers of upward and downward steps in the whole traces show a stronger dependency on actin concentration. For high concentrations of 1 μM or more, 20 to 30 upward steps have been determined, whereas for lower concentrations, the number of upward steps

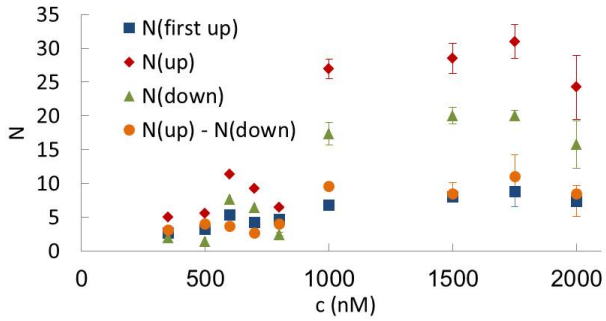

Figure 3.14: **Mean number of steps.** Measurement duration 13 min, for 350 nM 25 min. Above 0.7 μM, error bars represent the standard deviation of the mean of 2 or 3 (1.5 μM) measurements.

is in the regime of 5 to 10.

Like the number of steps, the fitted rates of all upward steps show an overall linear increase with concentration (Fig. 3.15). At the highest measured concentrations, the rates of the second and onwards steps seem to decrease. In this regime, the on-rates estimated from the inverse of the mean dwell times reach up to 0.1 to 0.2 s^{-1}, which is half or more of the value of the imaging rate (Fig. 3.16 A). As shown in the simulations, here the ability to recover the correct rates and number of kinetic intermediates reaches its limits. For the determination of the rate constants, concentrations above 1.5 μM and the data points for 1.25 μM actin have been excluded. The latter differ from the other measurements both in the rates and in the number of steps, and in the appearance of the traces (Appendix II). The rate constants for the first and the second step step have been determined to be 0.60 $\mu M^{-1}s^{-1}$ and 0.50 $\mu M^{-1}s^{-1}$, respectively.

The fitted rates for polymerization and depolymerization are overall similar (Fig. 3.16). Both show a linear increase with actin concentration in the range up to 1 μM. At higher concentrations, the polymerization and depolymerization rates show no further increase. The mean arrival times here show values around 20 s, which in principal would still be in a resolvable range. However, at these high concentrations, the mean step size can go up to 50 or 60, which is slightly too high compared to lower concentrations and DNA bleaching measurements (Appendix I). Therefore, for the linear fit, only concentrations up to 800 nM have been included. A rate constant of

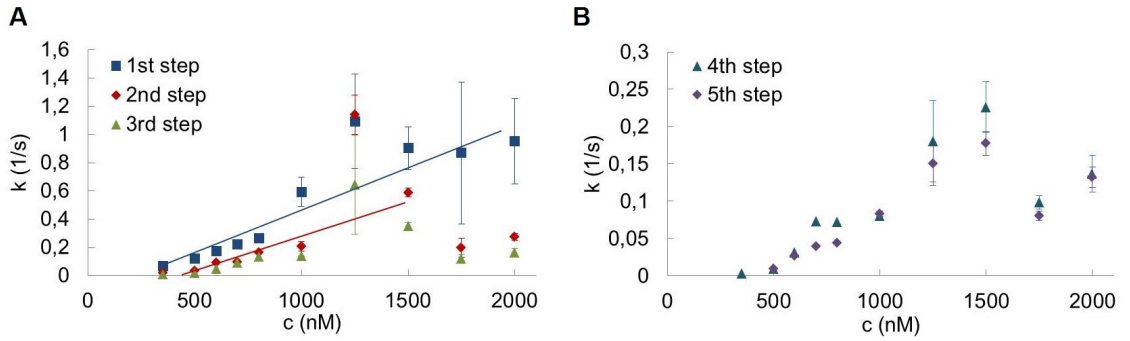

Figure 3.15: **Fitted on-rates vs. actin concentration. A:** Steps 1 to 3. Straight lines: linear fit y=ax + b (data at 1.25 μM has been excluded). First step: a = 0.00060, b = -0.15 R^2 = 0.94, second step: a = 0.00050, b = -0.2, R^2 = 0.94. **B:** steps 3 and 4. Above 0.7 μM, error bars represent the standard deviation of the mean of 2 or 3 (1.5 μM) measurements.

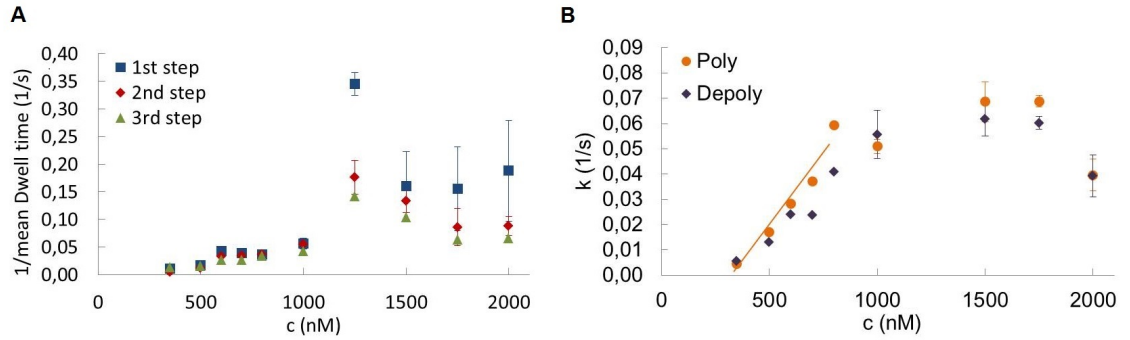

Figure 3.16: **Estimated rates for the first three steps and fitted rates for polymerization and depolymerization. A:** Rates estimated from the mean of the dwell time distribution, **B:** Fitted rates for polymerization and depolymerization. Straight line: linear fit y=ax + b, polymerization: a = 0.00012, b = -0.04, R^2 = 0.96. Above 0.7 μM, error bars represent the standard deviation of the mean of 2 or 3 (1.5 μM) measurements.

0.12 $\mu M^{-1}s^{-1}$ has been estimated for polymerization.

As discussed in the theory section, the inverse of the randomness parameter r corresponds to the minimum number of underlying kinetic states n_{min} of a step. Additionally, n has been fitted to the distribution as described in the analysis section.

For polymerization steps, n_{min} and n are around 1.0 or 1.3, respectively, for all measured actin concentrations (Fig. 3.17). The first step, however, reaches values up to $n_{min} = 6.1 \pm 1.7$ or $n = 9.7 \pm 0.3$ (standard deviation of the mean, 2 independent measurements) at 1 μM. At low concentrations, n_{min} starts with a value of 1, and the fitted number of states is about 4 to 5. At high concentrations, n_{min} goes back

to 2 to 3, n to 6. The second and onward steps show values of n_{min} between 1 and 2. The second step seems to show some increase with concentration and reaches a value of about 3 at 1.5 μM. The concentration dependency of the second and third step is more pronounced in the fitted n, where values increase almost linearly from about 2 to 3 or 4 at 1.5 μM, respectively.

The determination of the arrival times for the first step is more error-prone than that of the subsequent steps because of the manual adding of the actin polymerization mix onto the waveguides. Whereas at low concentrations, one or two seconds do not shift the histogram cosiderably compared to the mean value, at higher concentrations the insecurity in the beginning of the measurement has a stronger effect. The shifting of the whole histogram towards higher values in the time axis results in lower values for r, and higher values for n. However, independent measurements similarly showed rather high values between 800 nM and 1.5 μM. The second and third step show reproducible results. The number of minimum kinetic intermediates for the arrival of the second actin monomer is around 1 at low concentrations, and around 2 at high concentrations, which could indicate an additional transition of the protein before the incorporation of the second monomer that becomes kinetically relevant at high concentrations.

Overall, gelsolin-mediated actin nucleation seems to include the addition of several actin monomers in the beginning of the growth phase. Whereas at lower concentrations up to 800 nM, filaments do not seem to grow very much beyond that intital increase or even lose monomers afterwards, at higher concentrations, further growth seems more favorable.

Latrunculin A is a drug that binds to monomeric actin and prevents succesfull filament formation (see theory section). With excess concentrations of LatA, both the initial upward steps and the netto upward steps stay below or around 5, even at high concentrations (Fig. 3.18 A). After the initial increase of intensity, traces show more downward than upward steps. Although the number of upward steps in the beginning is low and the filament is composed of very little monomers at the end of the measurement, the number of all upward and downward steps is high (up to

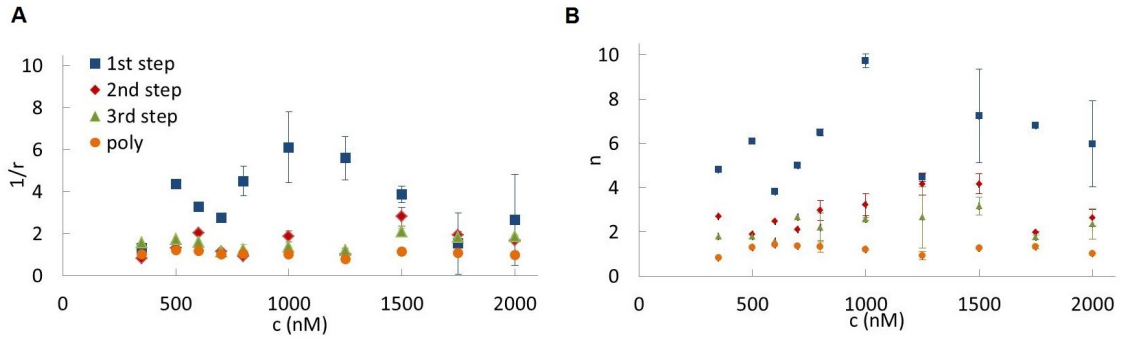

Figure 3.17: **n_{min} and n vs. actin concentration. A:** The inverse of the randomness paramter $1/r = n_{min}$. **B:** Fitted number of kinetic intermediates in a step n. Above 700 nM actin, error bars respresent the standard deviation of the mean of 2 or 3 (1.5 μM) measurements.

about 20) and depends on concentration.

At 1.5 μM, a negative number of netto upward steps has been determined by the step finding algorithm. The traces of this measurement show a very quick intensity increase, followed mostly by depolymerization. For this reason, the arrival time distributions for the individual upward steps could not be fitted, because there are hardly any upward steps before the first downward step (Appendix II). The mean step size for these traces has a value of 154, which is far off the values of the DNA bleaching and other actin measurements (Appendix I). It seems that in this particular measurement, actin monomers have been incorporated very fast in the beginning, so that the individual steps could not be resolved any more, even with the assumption of double and triple steps.

The on-rates for the first three upward steps, as well as the depolymerization and polymerization rates are slightly smaller than the rates of measurements without LatA (polymerization: 0.063 at 2 μM versus 0.069 $\pm$ 0.002 at 1.75 μM, standard deviation of the mean, 2 measurements), and show similar trends (Fig. 3.18 B). The rate constants for the first and the second step are at 0.31 $\mu M^{-1}s^{-1}$ and 0.27 $\mu M^{-1}s^{-1}$, respectively. The polymerization rate constant has been determined to be at 0.03 $\mu M^{-1}s^{-1}$.

Like without LatA, the shape of the arrival time distribution of the first step results in rather high values for n and n_{min}. At the lowest measured actin concentration

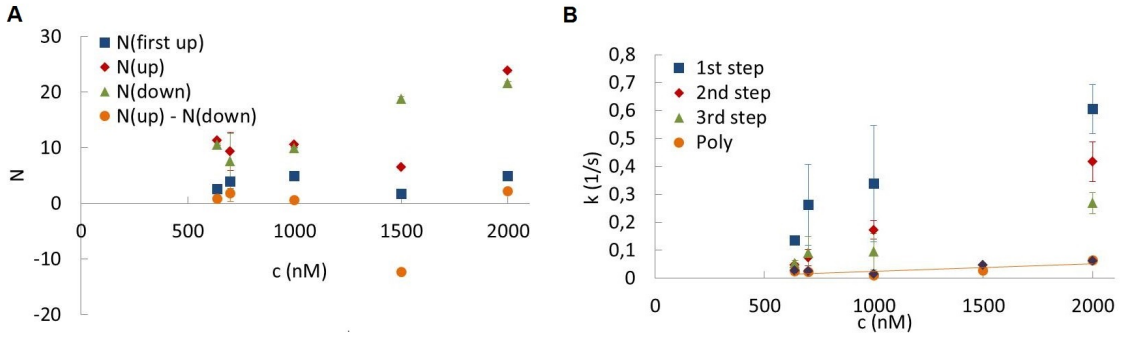

Figure 3.18: **Effect of LatA. A:** Mean number of steps (measurement duration 13 min). **B:** Fitted rates. Error bars represent 95% confidence intervals of the fit. Error bars for 700 nM represent the standard deviation of 2 measurements. For 1.5 μM, the dwell time distributions of the individual upward steps could not be fitted.

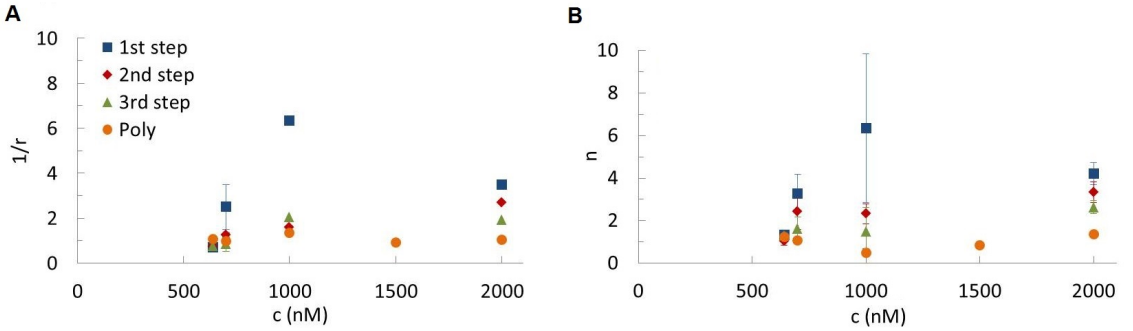

Figure 3.19: **Effect of LatA: number of kinetic intermediates. A:**: Minimum number of kinetic intermediates n_{min}, **B:** Fitted number of kinetic intermediates n. Error bars represent 95% confidence intervals of the fit. Error bars for 700 nM represent the standard deviation of 2 measurements. For 1.5 μM, the dwell time distributions of the individual upward steps had too little statistics.

however, the values for n and n_{min} are slightly above 1 (Fig. 3.19). For the second step, n lies between 2 and 3. The minimum as well as the fitted number of kinetic intermediates for the third step and the pooled polymerization steps have values between 1 and 2. Here, at 1 μM, the n_{min} is larger than the fitted n. As the 95% confidence intervals are very small and inside the data points, it is assumed that some outlying arrival times shift the ratio of the variance over the mean.

Both with and without LatA, traces show a dynamic behavior with high numbers of upward and downward steps. Whereas without LatA, more and more monomers stay bound to the filament at higher concentrations, with Latrunculin, no more than

two monomers are bound to gelsolin at the end of the traces.

3.3 Barbed End Nucleation

3.3.1 Nucleation on biotinylated Actin

To measure direct actin nucleation, biotinylated monomeric actin was used as tethering protein. Filament elongation is possible in both directions, however, since the barbed end shows faster kinetics, mainly elongation along that direction is expected. Experiments have been performed in a concentration range from 250 nM to 1 μM. Measurement durations varied from 13 min at higher actin concentrations to up to one hour at the very low concentration regime. Because of the very different measurement times, only the intitial increase before the first downward step is considered here. In contrast to nucleation mediated by gelsolin, the mean number of those steps shows no concentration dependence, but stays mostly between 3 and 4 (Fig. 3.20). Nevertheless, the fitted rates for upward steps and depolymerization increase with concentration (Fig. 3.21). The first step shows some deviation, but the second step, third and polymerization steps show an overall linear dependency on actin concentration. The estimated rates from the inverse of the mean show smaller values, similar to what has been seen with gelsolin. However, the values for the addition of the first free actin monomer is about a magnitude smaller than with gelsolin, and the polymerization rates about a factor of 3.

The number of kinetic intermediates for the third step as well as the polymerization and depolymerization steps stays at about two over the whole concentration range (Fig. 3.20 B). For the second step, n has values between three and four. For the first step, some measurements show values about two, but larger values up to 8 have been determined as well.

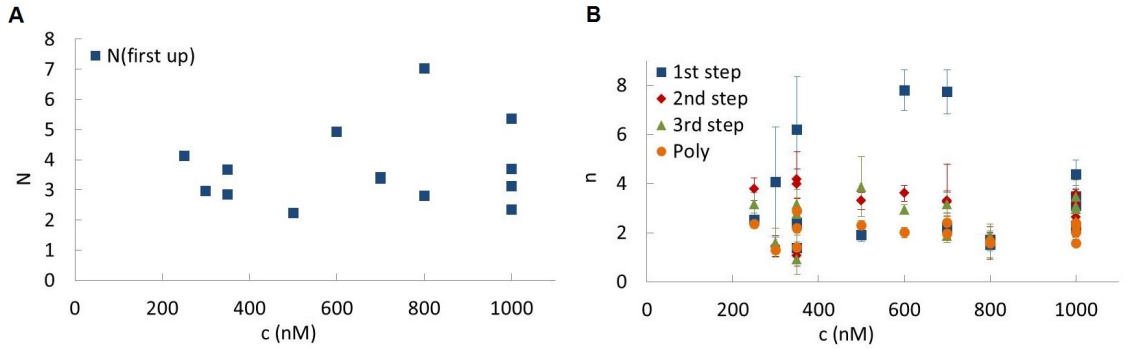

Figure 3.20: **The initial increase in actin nucleated traces and the number of kinetic intermediates. A:** Mean number of upward steps before the first downward step in a trace. The standard deviation of the mean is inside data points. **B:** Fitted number of kinetic intermediates n. Error bars represent 95% confidence intervals of the fit.

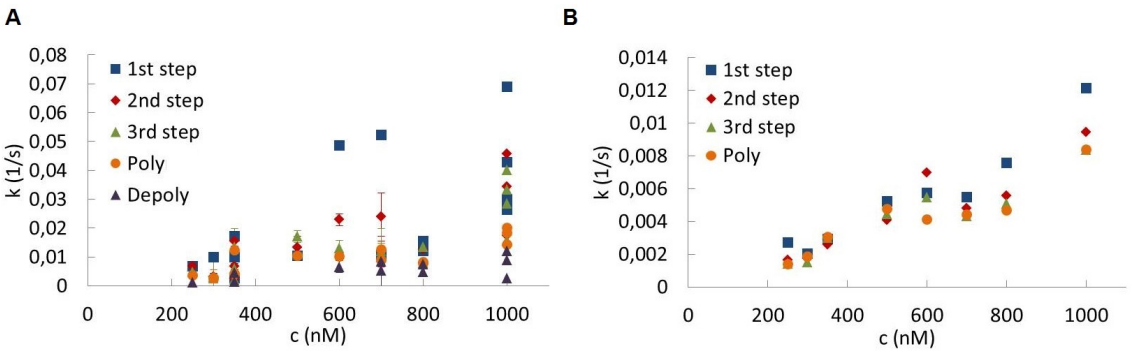

Figure 3.21: **Fitted and estimated rates. A:** Fitted rates. Error bars represent 95% confidence intervals of the fit.**B:** The inverse of the mean arrival times for the indivitual steps, mean of independent measurements, standard deviation of the mean is inside data points.

3.3.2 DNase I mediated Nucleation

As the DNase binding loop on actin is at the pointed end, elongation with DNase I as tethering protein takes place on the barbed end only. Four actin concentrations have been measured ranging from 300 to 1000 nM. Concerning the mean number of steps, contradicting results have been found for different measurements (Fig. 3.22 A). For some measurements, high numbers of upward and downward steps have been found, whereas others show very little downward steps. Consequently, the numbers of upward steps and the steps of the initial increase before the first downward step do not differ much in those measurements. Besides, the number of upward steps seems to decrease with actin concentration. These different findings could be sorted into two measurement periods with different actin batches. As the second actin batch and the photococktail have been tested with total internal reflection microscopy within not more than two weeks distance to the experiments, only these measurements are considered (Fig. 3.22 B).

Here, the number of all depicted types of steps increase with actin concentration, at least up to 0.7 μM. As with pointed end elongation on gelsolin, traces seem to be very dynamic with many upward and downward steps, but a netto number of steps that does not differ much from the intial increase of the traces. Those steps show numbers of up to 4, which is comparable to measurements with biotinylated gelsolin in this concentration range as well. However, whereas the dynamic range with a lot of association and dissociation of actin monomers occurs at concentrations above 1 μM with gelsolin, here the overall number of upward and downward steps in the traces reaches high values already at lower concentrations, i.e. 500 nM.

The rates for the first upward step increase linearly from 0.009 s^{-1} at 300 nM to 0.12 s^{-1} at 700 nM (Fig. 3.23 A). At 1 μM, a comparatively high rate of 0.7 s^{-1} has been determined. The second transition as well as polymerization and depolymerization have similar rates and are much slower than the first transition (Fig. 3.23 B). All of them show an overall linear increase over the full concentration range. At lower concentrations, the depolymerization rate is very similar, but slightly lower than the polymerization rate, whereas at higher concentrations, polymerization is faster.

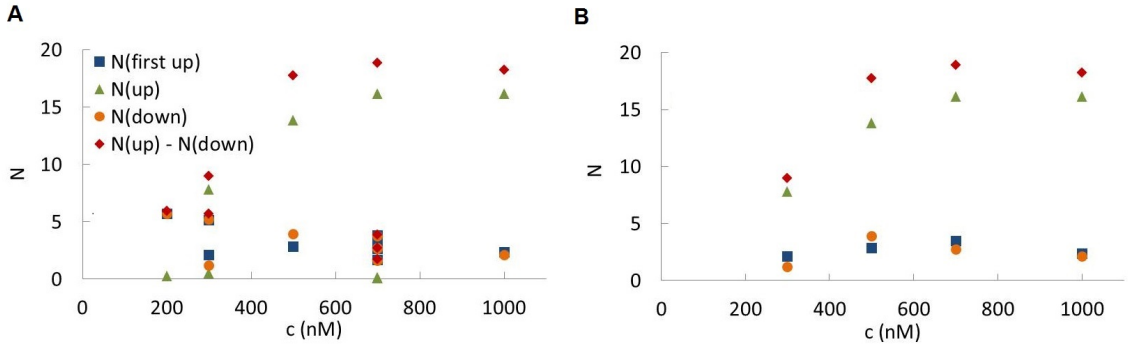

Figure 3.22: **Mean number of steps. A:** all measurements, **B:** only measurements of one actin batch. The standard deviation of the mean is inside data points.

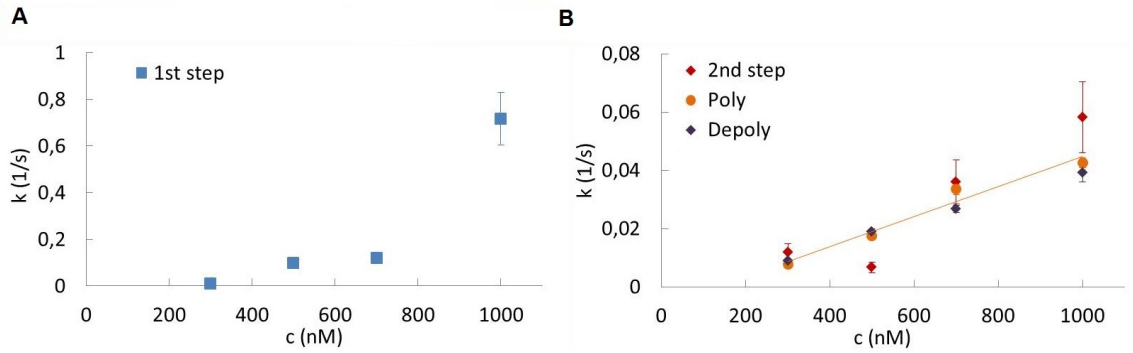

Figure 3.23: **Fitted rates for DNase I mediated nucleation. A:** first step, **B:** second step step, polymerization and depolymerization. Straight line: linear fit (y=ax+b). For polymerization: a = $5{\cdot}10^{-7}$, b = -0.007, R^2 = 0.97. Error bars represent 95% confidence intervals.

The rate constant for polymerization has been determined to be at 0.05 μMs^{-1}.

For the polymerization steps, both n_{min} and n are around one for all concentrations (Fig. 3.24). For the third transition, n_{min} stays at one for all concentrations as well, whereas n shows a larger spread. For the second step, n is slightly above one for almost all concentrations, whereas n_{min} has smaller values for 500 nM and 1 μM. Both n and n_{min} have values below 1 for the first step. n seems to have a trend towards higher values with concentration, however, for 1 μM, the distribution was fitted with an exponential decay which would technically have n = 1, but does not include it in the fit. Values for r larger than one, or correspondingly an n_{min} smaller than one can be associated with parallel pathways (see theory section).

With LatA, filament formation is inhibited (table 3.6). Nevertheless, many upward and downward steps are detected, similarly to what has been measured for binding

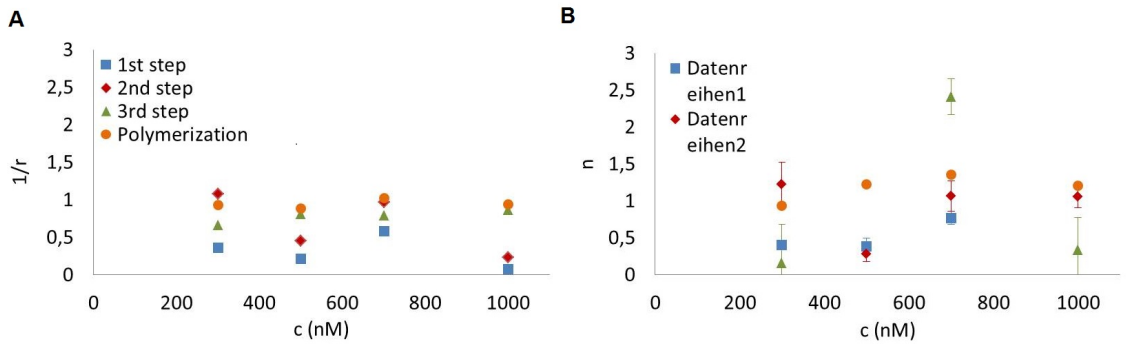

Figure 3.24: **n_{min} and n for DNase I mediated nucleation. A:** minimum number of kinetic intermidates $n_{min} = 1/r$, **B:** Fitted number of underlying kinetic intermediates. For 500 nM, the arrival time distribution of the third step could not be fitted satisfactoringly. Error bars represent 95% confidence intervals.

Table 3.6: **Effect of LatA on barbed end nucleation.** 700 nM actin concentration, one measurement. The mean number of upward steps before the first downward step, the mean number of all upward and all downward steps in a trace and their difference are displayed.

$N_{first\ up}$	N_{up}	N_{down}	N_{up}-N_{down}
2.6	19	19	0.9

of incoming actin monomers with bound LatA to the pointed end.

4 Discussion

For pointed end nucleation via gelsolin and barbed end nucleation via DNase I or actin, the measured traces showed an initial increase in intensity, followed by a dynamic region, which can either lead to succesfull filament elongation, or the disruption of the newly formed filament. The dynamic region where many association and dissociation events are detected occurs at concentrations of about 100 to 200 nM above the critical concentration for barbed end or pointed end elongation, respectively. When Latrunculin A is added to the actin monomers, a similar amount of association and dissociation events as without Latrunculin has been determined. However, with Latrunculin, only one or two actin monomers stay bound at the end of the measurement, independently on concentration. As the crystal structure of actin with bound Latrunculin implied, either ATP hydrolysis or flattening of the monomer or both events are inhibited by LatA [58]. Therefore, it is assumed that the dynamic range of the traces show many unstable binding events. Only when the previously bound actin monomers underwent the transitions blocked by LatA, additional monomers can bind stably and build a new filament.

The kinetics of the process have been determined at various concentrations. For concentrations higher than 1.5 μM, the fitted rates as well as the estimated rates from the mean arrival times of the second and onwards step seemed to level off and show no further increase with concentration. The first step, in contrast, still shows a linear increase. As shown in the simulations, step-finding algorithms have difficulties in detecting the underlying arrival time distribution for rates faster than about half of the measurement cycle time. Only when the fast step was set to be the first step, arrival times have been recovered. For that reason, it could be that at these concentrations, kinetics of the second and onwards steps get too fast to be resolvable by the Salapaka algorithm. It is therefore not believed that an actual saturation of the kinetics at these actin concentrations occurs. Alternatively, it could also be that with increasing concentration, barbed end growth in solution

has more and more impact on the actual monomer concentration. If the effect of polymerization in solution is considerable, the effective monomer concentration would be time-dependent in the beginning of the measurement. When at very early time points the effective monomer concentration still is similar to the assumed monomer concentration, the first step of gelsolin-mediated nucleation would be least effected.

With LatA bound to the actin monomers, polymerization in solution should be blocked. The LatA measurements with gelsolin as tethering protein roughly show a linear increase of the determined rates also at high concentrations. The further increase of the rates measured with LatA indicate that competition with polymerization in solution is partly responsible for the not further increasing rates. However, as the critical concentration for barbed end elongation is at 120 nM [3], this competition should have an effect also at lower concentrations. The slope of this increase is smaller than the slope of the rates measured without LatA at low concentrations. Accordingly, the determined rate constants for polymerization differ for measurements with and without LatA (0.03 vs. 0.12 $\mu M^{-1}s^{-1}$). This discrepancy was not expected as LatA does not induce dramatic changes in the actin monomer structure itself [58]. Apart from the limitations of step-finding, another explanation for the discrepancy between the polymerization rates could be the definition of polymerization as it is used here, i.e. the pooled upward steps after the first downward step. The first downward step occurs in average after 2 to 4 s after the beginning of the measurement with LatA, but only after 40 to 400 s without LatA. Whereas without LatA, the assumption that the upward steps afterwards are polymerization steps is probably true in most cases, with LatA the polymerization steps could be a mixture of an actin monomer binding to gelsolin or to another actin monomer. Measurements of the rates with LatA at lower concentrations would be interesting to determine the rate constant at lower concentrations.

For DNase I-mediated and actin-mediated nucleation, only concentrations up to 1 μM have been measured. Because of the very fast kinetics at higher concentrations, the filaments started to grow before the measurement could be started. The intergration of the zero-mode waveguides in a flow system would help to better

control the timepoint of the beginning of the measurement.

From the fitted rates at concentrations up to 1.5 μM, the rate constants have been determined. For gelsolin-mediated pointed end polymerization, a rate constant of 0.12 $\mu M^{-1}s^{-1}$ has been determined, which happens to be exactly the value described in literature [48]. The rate constant for the binding of the first actin monomer to gelsolin has been determined to be at 0.60 $\mu M^{-1}s^{-1}$. For the 1:1 gelsolin:actin complex formation a rate constant of 0.02 $\mu M^{-1}s^{-1}$ has been described in literature [48], and 20 $\mu M^{-1}s^{-1}$ for the binding of the second actin monomer [52]. For the formation of the 1:2 complex, here a rate constant of 0.50 $\mu M^{-1}s^{-1}$ has been determined. Whereas in the literature, binding of the first actin monomer is very slow compared to the formation of the 1:2 complex, here the reported difference of three magnitudes in the rate constants of the first and second actin monomer binding to gelsolin could not be seen. The confined volume of the waveguides is probable to influence the diffusion kinetics, however, these large discrepancies can not be explained by that. The described rate constants have been determined in bulk measurements with filamentous actin, actin monomers and gelsolin, which should be quite a dynamic system. In contrast to that, here the arrival times of single actin monomers to one gelsolin are measured directly. For the polymerization rate, the found value is in good agreement to the literature [48].

Both the number of downward steps and their rate are concentration-dependent. The bleaching rate at the used laser power of 5 mW has been determined to be at 0.0087 ± 0.0004 (standard deviation of the mean, three measurements), which is far lower than the determined depolymerization rates. However, the waiting time for the depolymerization rate are determined with respect to the timepoint of the arrival of the previous step, but every labeled actin monomer in the filament could possibly bleach. Therefore, with more labeled monomers in a filament, the probability for a bleaching event should also increase. Simulations to find out if that effect is strong enough to be responsible for the concentration-dependency of the depolymerization rate would be interesting.

Using the principles of statistical kinetics, the number of kinetic intermediates for

the arrival times of the different actin monomers could be determined. For polymerizaiton, the number of underlying kinetic intermediates is about one for all measured concentrations for gelsolin-mediated pointed end and DNase I- mediated barbed end elongation. The flattening of the actin monomer after or upon incorporation into a filament would result in an additional state, however, this could only be observed in the arrival time distribution when the kinetics of this transition are relevant at the measured concentrations. Therefore, it could be that flattening occurs fast in comparison to the addition of actin monomers.

The measurements with biotinylated actin showed numbers about two for the polymerization steps. In these measurements, filaments can grow in both directions, which could result in a change in the arrival time distribution. However, this would enlargen the variance of the distribution, which would result in a higher randomness parameter and therefore in a smaller number of kinetic intermediates.

The number of underlying kinetic intermediates showed some variation for the binding of the first monomer. This could represent conformational changes in gelsolin due to its interaction with Ca^{2+}. However, at the beginning of the measurement gelsolin has been for about 15 min in G-buffer that contains enough Ca^{2+} to undergo the required conformational changes for actin binding. The manual adding of actin to the waveguides leads to a certain insecurity of one or two seconds concerning the start of the measurement, i.e. time 0. Additionally, the number of kinetic intermediates for the first step varied most between different step-finding algorithms.

For the arrival times of second actin monomer to gelsolin, the minimum number of kinetic states was determined to be little below 2. It is believed that actin binding to gelsolin can trigger the binding of additional Ca^{2+} [40], which could be an explanation for the additional state. The binding of the third actin monomer to the 1:2 gelsolin:actin complex shows minimum 2 to 3 kinetic states. This is in agreement with the observed rearrengement of actin involving the DNase binding loop and the C-terminums of the second bound actin monomer after binding to gelsolin [47].

For the binding of the first actin monomer to DNase I, randomness parameters of

about 2 were found, which is associated with multiple pathways. Different conformations of the DNase binding loop in actin have been proposed [11, 15, 16], which could result in different pathways dependent on the conformational state of the actin monomer.

Overall, the meachnisms of actin nucleation seems to involve at least one conformational change per actin molecule. For DNase I mediated barbed end nucleation, more than one pathway for the binding of the first actin monomer could be possible.

5 Summary

In this thesis, the process of actin filament nucleation has been visualized directly. The confined observation volume in zero-mode waveguides made it possible to study the required concentrations in the micromolar range via fluorescent microscopy. The incoming labeled actin monomers have been measured in an intensity-time trace. Different step-finding algorithms have been tested in simulations and control experiments. The Salapaka algorithm has been found to most reliably find the arrival times of the actin monomers and the number of upward and downward steps in the noise-overlayed traces.

With the use of biotinylated gelsolin, actin and DNase I as tethering proteins at the bottom of the waveguides, barbed end as well as pointed end elongation could be studied separately. Above the critical concentration, the growing filaments showed a very dynamic range with many association and dissociation events.

Bibliography

[1] L. Blanchoin, R. Boujemaa-Paterski, C. Sykes, and J. Plastino. Actin dynamics, architecture, and mechanics in cell motility. *Physiological Reviews*, 94:235–263, 2014.

[2] T. Oda, M. Iwasa, T. Aihara, Y. Maeda, and A. Narita. The nature of the globular- to fibrous-actin transition. *Nature*, 457:441–445, 2009.

[3] T. Pollard. Rate constants for the reactions of ATP- and ADP-actin with the ends of actin filaments. *The Journal of Cell Biology*, 103:2747–2754, 1986.

[4] S. Hell and J. Wichman. Breaking the diffraction resolution limit by stimulated emission: stimulated-emission-depletion-microscopy. *Opt. Lett.*, 19:780–782, 1994.

[5] E Betzig, G. Patterson, R Sougrat, Lindwasser O., S. Olenych, J. Bonifacino, M. Davidson, Lippincott-Schwartz J., and H. Hess. Imaging intracellular fluorescent proteins at nanometer resolution. *Science*, 313:642 – 1645, 2006.

[6] R. Dickson, A. Cubitt, R. Tsien, and W. Moerner. On/off blinking and switching behaviour of single molecules of green fluorescent protein. *Nature*, 388:355–358, 1997.

[7] W. Moerner and L. Kador. Optical detection and spectroscopy of single molecules in a solid. *Phys. Rev. Lett.*, 62:2535–2538, 1989.

[8] M. J. Levene, J. Korlach, S. W. Turner, M. Foquet, H. G. Craighead, and W. W. Webb. Zero-mode waveguides for single-molecule analysis at high concentrations. *Science*, 299:682–686, 2003.

[9] J. Moffitt and C. Bustamate. Extracting signal from noise: kinetic mechanisms from a michaelis-menten-like expression for enzymatic fluctuations. *FEBS Journal*, 281:498–517, 2014.

[10] W. Kabsch, H. Mannherz, D. Suck, E. Pai, and K. Holmes. Atomic structure of the actin:DNase I complex. *Nature*, 347:37–44, 1990.

[11] P. Graceffa and R. Dominguez. Crystal Structure of Monomeric Actin in the ATP State: structural basis of nucleotide dependent actin dynamics. *Journal of Biological Chemistry*, 278:34172–34180, 2003.

[12] L. Otterbein, P. Graceffa, and R. Dominguez. The Crystal Structure of Uncomplexed Actin in the ADP State. *Science*, 293:708–711, 2001.

[13] L. Belmont, A. Orlova, D. Drubin, and E. Egelman. A change in actin conformation associated with filament instability after Pi release. *PNAS*, 96:29–34, 1999.

[14] E. Korn, M. Carlier, and D. Pantaloni. Actin polymerization and atp hydrolysis. *Science*, 238:638–644, 1987.

[15] M. Rould, Q. Wan, P. Joel, S. Lowey, and K. Trybus. Crystal Structures of Expressed Non-polymerizable Monomeric Actin in the ADP and ATP States. *Journal of Biological Chemistry*, 281:31909–31919, 2006.

[16] J. Pfaendtner, D. Branduardi, M. Parrinello, T. Pollard, and G. Voth. Nucleotide-dependent conformational states of actin. *PNAS*, 106:12723–12728, 2009.

[17] L. Blanchoin and T. Pollard. Hydrolysis of ATP by polymerized actin depends on the bound divalent cation but not profilin. *Biochemistry*, 41:597–602, 2002.

[18] S. Vorobiev, B. Strokopytov, D. Drubin, C. Frieden, S. Ono, J. Condeelis, P. Rubenstein, and S. Almo. The structure of nonvertebrate actin: Implications for the ATP hydrolytic mechanism. *PNAS*, 100:5760–5765, 2003.

[19] K. Holmes, D. Popp, W. Gebhard, and W. Kabsch. Atomic model of the actin filament. *Nature*, 347:44–49, 1990.

[20] K. Holmes, I. Angert, F. Kull, W. Jahn, and R. Schröder. Electron cryomicroscopy shows how strong binding of myosin to actin releases nucleotide. *Nature*, 425:389–390, 2003.

[21] A. Wegner. Head to tail polymerization of actin. *Journal of molecular biology*, 108:139–150, 1976.

[22] K. Holmes. Actin in a twist. *Nature*, 457:423–427, 2009.

[23] S. Nag, M. Larsson, R. Robinson, and L. Burtnick. Gelsolin: The tail of a molecular gymnast. *Cytoskeleton*, 70:360–384, 2013.

[24] H. Yin and T. Stossel. Control of cytoplasmic actin gel-sol transformation by gelsolin, a calcium-dependent regulatory protein. *Nature*, 281:583–586, 1979.

[25] H. Yin, J. Hartwig, K. Maruyama, and T. Stossel. Calcium-control of actin filament length. *J. Biol. Chem.*, 256:9693–9697, 1981.

[26] L. Burtnick, E. Koepf, J. Grimes, Y. Jones, D. Stuart, P. McLaughlin, and R. Robinson. The crystal structure of plasma gelsolin: Implications for actin severing, capping, and nucleation. *Cell*, 90:661–670, 1997.

[27] H. Choe, L. Burtnick, M. Mejillano, H. Yin, R. Robinson, and S. Choe. The calcium activation of gelsolin: Insights from the 3Å structure of the g4–g6/actin complex. *Journal of Molecular Biology*, 324:691 – 702, 2002.

[28] M. Way, J. Gooch, B. Pope, and A. Weeds. Expression of human plasma gelsolin in Escherichia coli and dissection of actin binding sites by segmental deletion mutagenesis. *The Journal of Cell Biology*, 109:593–605, 1989.

[29] L. Burtnick, D. Urosev, E. Irobi, K. Narayan, and R. Robinson. Structure of the N-terminal half of gelsolin bound to actin: roles in severing, apoptosis and FAF. *EMBO*, 23:2713–2722, 2004.

[30] Ashish, M. Paine, P. Perryman, L. Yang, H. Yin, and J. Krueger. Global structure changes associated with ca2+ activation of full-length human plasma gelsolin. *J Biol Chem.*, 282:25884–25892, 2007.

[31] R. Robinson, M. Mejillano, V. Le, L. Burtnick, H. Yin, and S. Choe. Domain movement in gelsolin: A calcium-activated switch. *Science*, 286:1939–1942, 1999.

[32] S. Kolappan, J. Gooch, A. Weeds, and P. McLaughlin. Gelsolin domains 4–6 in active, actin-free conformation identifies sites of regulatory calcium ions. *Journal of Molecular Biology*, 329:85 – 92, 2003.

[33] K. Narayan, S. Chumnarsilpa, H. Choe, E. Irobi, D. Urosev, U. Lindberg, C. Schutt, L. Burtnick, and R. Robinson. Activation in isolation: exposure of the actin-binding site in the c-terminal half of gelsolin does not require actin. *FEBS Letters*, 552:82–85, 2003.

[34] H. Wang, S. Chumnarnsilpa, A. Loonchanta, Q. Li, Y. Kuan, S. Robine, M. Larsson, I. Mihalek, L. Burtnick, and R. Robinson. Helix straightening as an activation mechanism in the gelsolin superfamily of actin regulatory proteins. *J Biol Chem.*, 284:21265–21269, 2009.

[35] B. Pope, S. Maciver, and A. Weeds. Localization of the calcium-sensitive actin monomer binding site in gelsolin to segment 4 and identification of calcium binding sites. *Biochemistry*, 34:1583–1588, 1995.

[36] S. Khaitlina, M. Walloscheck, and H. Hinssen. Calcium-Induced Conformational Changes in the C-Terminal Half of Gelsolin Stabilize Its Interaction with the Actin Monomer. *Biochemistry*, 43:12838–12845, 2004.

[37] J. Bryan and S. Hwo. Definition of an N-terminal actin-binding domain and a C-terminal Ca2+ regulatory domain in human brevin. *The Journal of Cell Biology*, 102:1439–1446, 1986.

[38] T. Hellweg, H. Hinssen, and W. Eimer. The ca2+-induced conformational change of gelsolin is located in the carboxyl-terminal half of the molecule. *Biophysical Journal*, 65:799–805, 1993.

[39] P. Allen and P. Janmey. Gelsolin displaces phalloidin from actin filaments. A new fluorescence method shows that both Ca2+ and Mg2+ affect the rate at which gelsolin severs F-actin. *J Biol Chem.*, 269:32916–32923, 1994.

[40] L. Selden, H. Kinosian, J. Newman, B. Lincoln, C. Hurwitz, L. Gershman, and J. Estes. Severing of F-actin by the amino-terminal half of gelsolin suggests internal cooperativity in gelsolin. *Biophys J.*, 75:3092–3100, 1998.

[41] J. Kiselar, P. Janmey, S. Almo, and M. Chance. Visualizing the Ca2+-dependent activation of gelsolin by using synchrotron footprinting. *Proceedings of the National Academy of Sciences*, 100:3942–3947, 2003.

[42] A. Ditsch and A. Wegner. Two low-affinity ca2+-binding sites of gelsolin that regulate association with actin. *FEBS*, 229:512–516, 1995.

[43] H. Kinosian, J. Newman, B. Lincoln, L. Selden, L. Gershman, and J. Estes. Ca2+ Regulation of Gelsolin Activity: Binding and Severing of F-actin. *Biophys J.*, 75:3101–3109, 1998.

[44] A. Weeds, J. Gooch, P. McLaughlin, B. Pope, M. Bengtsdotter, and R. Karlsson. Identification of the trapped calcium in the gelsolin segment 1—actin-complex: Implications for the role of calcium in the control of gelsolin activity. *FEBS Letters*, 360:227 – 230, 1995.

[45] J. Bryan and M. Kurth. Actin-gelsolin interactions. evidence for two actin-binding sites. *Journal of Biological Chemistry*, 259:7480–7, 1984.

[46] J. Bryan. Gelsolin has three actin-binding sites. *The Journal of Cell Biology*, 106:1553–1562, 1988.

[47] S. Khaitlina and H. Hinssen. Conformational changes in actin induced by its interaction with gelsolin. *Biophysical Journal*, 73:929–937, 1997.

[48] N. Selve and A. Wegner. ph-dependent rate of formation of the gelsolin-actin complex from gelsolin and monomeric actin . *Eur. J. Biochem.*, 168:111–115, 1987.

[49] B. Pope, J. Gooch, and A. Weeds. Probing the effects of calcium on gelsolin. *Biochemistry*, 36:15848–15855, 1997.

[50] K. Lin, M. Mejillano, and H. Yin. Ca2+ regulation of gelsolin by its carboxyl-terminal tail. *Journal of Biological Chemistry*, 2000.

[51] S. Khaitlina and Hinssen. H. Ca-dependent binding of actin to gelsolin. *FEBS Letters*, 521:14 – 18, 2002.

[52] B. Schoepper and A. Wegner. Rate constants and equilibrium constants for binding of actin to the 1:1 gelsolin-actin complex. *FEBS*, 202:1127–1131, 1991.

[53] H. Mannherz, R. Goody, M. Konrad, and E. Nowak. The interaction of bovine pancreatic deoxyribonuclease I and skeletal muscle actin. *Eur. J. Biochem.*, 1979.

[54] R. Crosbie, C. Miller, P. Cheung, T. Goodnight, A. Muhlrad, and E. Reisler. Structural connectivity in actin: effect of C-terminal modifications on the properties of actin. *Biophys. J.*, 1994.

[55] I. Kuznetsova, O. Antropova, K. Turoverov, and S. Khaitlina. Conformational changes in subdomain I of actin induced by proteolytic cleavage within the DNase I-binding loop: energy transfer from tryptophan to AEDANS. *FEBS Lett.*, 383:105–108, 1996.

[56] I. Spector, N. Shochet, Y. Kashman, and A. Groweiss. Latrunculins: novel marine toxins that disrupt microfilament organization in cultured cells. *Science*, 1983.

[57] M. Coué, S. Brenner, I. Spector, and E. Korn. Inhibition of actin polymerization by latrunculin A. *FEBS Letters*, 213:316–318, 1987.

[58] W. Morton, K. Ayscough, and P. LcLaughlin. Latrunculin alters the actin-monomer subunit interface to prevent polymerization. *Nature Cell Biology*, 2:376–378, 2000.

[59] S. Rennebaum and A. Caflisch. Inhibition of interdomain motion in g-actin by the natural product latrunculin: A molecular dynamics study. *Proteins: Structure, Function, and Bioinformatics*, 80:1998–2008, 2012.

[60] K. Huang and A. Barron. Fluorescence Characterization and its Application in DNA Detection, May 2013.

[61] P. Zhu and H. G. Craighead. Zero-mode waveguides for single-molecule analysis. *Annual Review of Biophysics*, 41:269–293, 2012.

[62] J. Wenger, P. Lenne, Popov E., H. Rigneault, J. Dintinger, and T. Ebbesen. Single molecule fluorescence in rectangular nano-apertures. *Opt. Express*, 13(18):7035–7044, 2005.

[63] M. Foquet, K. Samiee, X. Kong, B. Chauduri, P. Lundquist, S. Turner, J. Freudenthal, and D. Roitman. Improved fabrication of zero-mode waveguides for single-molecule detection. *Journal of Applied Physics*, 103:034301, 2008.

[64] J. Korlach, P. Marks, R.. Cicero, J. Gray, L. Murphy, D. Roitman, T. Pham, G. Otto, M. Foquet, and S. Turner. Selective aluminum passivation for targeted immobilization of single dna polymerase molecules in zero-mode waveguide nanostructures. *Proceedings of the National Academy of Sciences*, 105:1176–1181, 2008.

[65] J. Moran-Mirabal and H. Craighead. Zero-mode waveguides: Sub-wavelength nanostructures for single molecule studies at high concentrations. *Methods*, 46:11 – 17, 2008.

[66] K. Samiee, M. Foquet, L. Guo, E. Cox, and H. Craighead. Lambda-repressor oligomerization kinetics at high concentrations using fluorescence correlation spectroscopy in zero-mode waveguides. *Biophysical Journal*, 88:2145 – 2153, 2005.

[67] J. Eid, A. Fehr, and J. et. al. Gray. Real-Time DNA Sequencing from Single Polymerase Molecules. *Science*, 323:133–138, 2009.

[68] T. Miyake, T. Tanii, H. Sonobe, R. Akahori, N. Shimamoto, T. Ueno, T. Funatsu, and I. Ohdomari. Real-time imaging of single-molecule fluorescence with a zero-mode waveguide for the analysis of protein-protein interaction. *Analytical Chemistry*, 80(15):6018–6022, 2008.

[69] M. Leutenegger, M. Goesch, A. Perentes, P. Hoffmann, O. Martin, and T. Lasser. Confining the sampling volume for fluorescence correlation spectroscopy using a sub-wavelength sized aperture. *Opt. Express*, 14:956–969, Jan 2006.

[70] K. Samiee, J. Moran-Mirabal, Y. Cheung, and H. Craighead. Zero mode waveguides for single-molecule spectroscopy on lipid membranes. *Biophysical Journal*, 90:3288– 3299, 2006.

[71] J. Wenger, H. Rigneault, J. Dintinger, D. Marguet, and P. Lenne. Single-fluorophore diffusion in a lipid membrane over a subwavelength aperture. *Journal of Biological Physics*, 32:SN1–SN4, 2006.

[72] M. Little and N. Jones. Sparse bayesian step-filtering for high-throughput analysis of molecular machine dynamics. In *ICASSP*, pages 4162–4165, 2010.

[73] B. Kalafut and K. Visscher. An objective, model-independent method for detection of non-uniform steps in noisy signals. *Computer Physics Communications*, 179:716 – 723, 2008.

[74] M. Little, B. Steel, F. Bai, Y. Sowa, T. Bilyard, D. Mueller, R. Berry, and N. Jones. Steps and bumps: precision extraction of discrete states of molecular machines using physically-based, high-throughput time series analysis. *Biophysical Journal*, 101:477–485, 2011.

[75] Gideon Schwarz. Estimating the dimension of a model. *Annals of Statistics*, 6:461 – 464, 1978.

[76] G. Chistol, S. Liu, C. Hetherington, J. Moffitt, S. Grimes, P. Jardine, and C. Bustamante. High degree of coordination and division of labor among subunits in a homomeric ring ATPase. *Cell*, 151:1017–1028, 2012.

[77] S. Kim, K. Koh, S. Boyd, and D. Gorinevsky. l1 trend filtering. *SIAM Reviews*, 51:339–360, 2007.

[78] T. Aggarwal, D. Materassi, R. Davison, T. Hays, and M. Salapaka. Detection of steps in single molecule data. *Cellular and Molecular Bioengineering*, 5:14–31, 2012.

[79] K. Svoboda, P. Mitra, and S. Block. Fluctuation analysis of motor protein movement and single enzyme kinetics. *Proc. Natl. Acad. Sci.*, 91:11782–11786, 1994.

[80] M. Schnitzer and S. Block. Statistical kinetics of processive enzymes. *Cold Spring Harb Symp Quant Biol*, 60:793 – 802, 1995.

[81] A. Samuel and H. Berg. Fluctuation analysis of rotational speeds of the bacterial flagellar motor. *Proc. Natl. Acad. Sci.*, 92:3502–3506, 1995.

[82] D. Aldous and L. Shepp. The least variable phase type distribution is Erlang. *Commum Statist Stochastic Models*, 3:467–473, 1987.

[83] S. Kou, B. Cherayil, W. Min, B. English, and X. Xie. Single-molecule michaelis-menten equations. *J. Phys. Chem. B*, 109:19068–19081, 2005.

[84] B. English, W. Min, A. Oijen, K. Lee, G. Luo, H. Sun, B. Cherayil, S. Kou, and X. Xie. Ever-fluctuating single enzyme molecules: Michaelis-Menten equation revisited. *Nat. Chem. Biol.*, 2:87–94, 2006.

[85] J. Moffitt, Y. Chemla, K. Aathavan, S. Grimes, P. Jardine, D. Anderson, and C. Bustamante. Inter-subunit coordination in a homomeric ring-ATPase. *Nature*, 457:446–450, 2009.

[86] J. Moffitt, Y. Chemla, and C. Bustamante. Mechanistic constraints from the substrate concentration dependence of enzymatic fluctuations. *Proc. Natl. Acad. Sci.*, 107:15739–15744, 2010.

[87] C. Aitken, R. Marshall, and J. Puglisi. An oxygen scavenging system for improvement of dye stability in single-molecule fluorescence experiments. *Biophysical Journal*, 94:1826–1835, 2008.

[88] I. Rasnik, S. McKinney, and T. Ha. Nonblinking and long-lasting single-molecule fluorescence imaging. *Nature Methods*, 3:891–893, 2006.

Appendix

Appendix I

Step Size distribution of the individual measurements.

Gelsolin

c(actin) (nM)	350	500	600	700	800	800	1000	1000	1250	1250	1500	1500
Step Size (a.u.)	24,5	18,9	35,2	41,7	24,8	44,4	53,4	43,1	64,9	48,2	62,8	64,3
c(actin) (nM)	1500	1750	1750	2000	2000							
Step Size (a.u.)	42,9	46,9	63,6	50,8	56,1							

Gelsolin + LatA

c(actin)	640	700	700	1000	1500	2000
Step Size (a.u.)	22,3	22,4	28,2	50,6	155	33,7

Actin

c(actin) (nM)	250	300	350	350	350	500	600	700	700	800	800	1000
Step Size (a.u.)	16,9	24,8	29,1	69,3	20,2	23,8	25,4	41,3	28,9	49,0	20,8	81,4
c(actin) (nM)	1000	1000	1000									
Step Size (a.u.)	22,0	28,4	27,0									

Dnase I

c(actin) (nM)	200	300	700	700	700	300	500	700	1000
Step Size (a.u.)	13,6	14,3	53,7	59,5	19,6	21,0	28,6	31,1	33,0

Dnase I + LatA

c(actin) (nM)	700
Step Size (a.u.)	32,5

Dnase I + Profilin

c(actin) (nM)	300	500	700	1000
Step Size (a.u.)	29,1	51,9	31,6	35,2

Appendix II

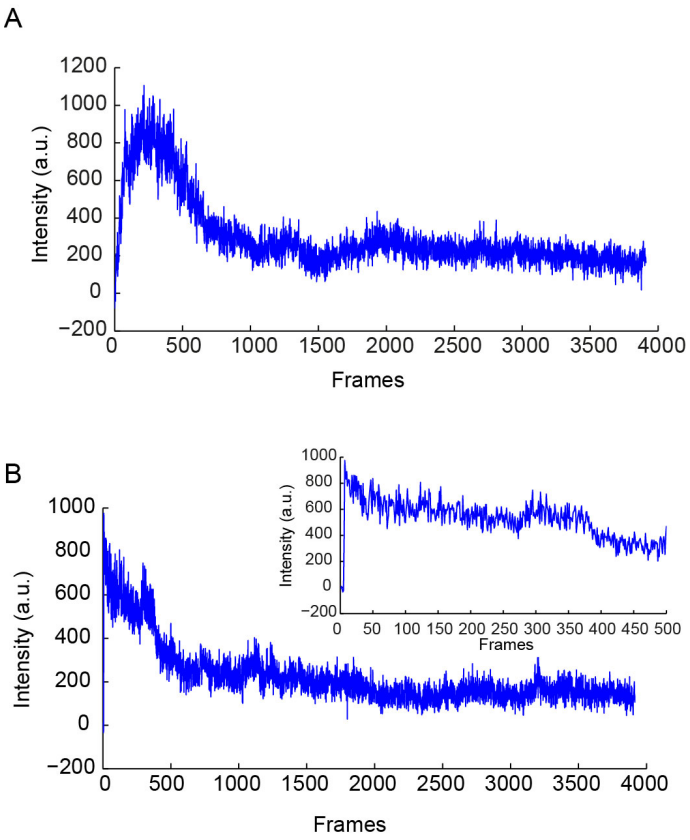

Abbildung 0.1: **Traces. A:** Gelsolin with 1.25 μM actin. **B:** Gelsolin with 1.5 μM actin and LatA.

Appendix III

Tabelle 0.1: **Simulations with the fast rate (0.05 s^{-1}) at different positions.** Previous steps at 0.03 s1−1. Recovered rate in s^{-1} and randomness paramenter r by the L1KV algorithm.

position of the fast step	rate	r
1	0.047	0.98
2	0.053	1.8
3	0.059	2.4